

Melting of Amphibole-bearing Wehrlites: an Experimental Study on the Origin of Ultra-calcic Nepheline-normative Melts

ETIENNE MÉDARD^{1*}, MAX W. SCHMIDT², PIERRE SCHIANO¹
AND LUISA OTTOLINI³

¹LABORATOIRE MAGMAS ET VOLCANS, UNIVERSITÉ BLAISE-PASCAL-CNRS, OPGC, 5 RUE KESSLER, F-63038 CLERMONT-FERRAND, FRANCE

²INSTITUT FÜR MINERALOGIE UND PETROGRAPHIE, ETH, SONNEGGSTRASSE 5, CH-8092 ZÜRICH, SWITZERLAND

³CNR-ISTITUTO DI GEOSCIENZE E GEORISORSE, SEZIONE DI PAVIA, VIA FERRATA 1, I-27100 PAVIA, ITALY

RECEIVED JANUARY 14, 2005; ACCEPTED OCTOBER 10, 2005
ADVANCE ACCESS PUBLICATION NOVEMBER 3, 2005

Olivine + clinopyroxene ± amphibole cumulates have been widely documented in island arc settings and may constitute a significant portion of the lowermost arc crust. Because of the low melting temperature of amphibole (~1100°C), such cumulates could melt during intrusion of primary mantle magmas. We have experimentally (piston-cylinder, 0.5–1.0 GPa, 1200–1350°C, Pt-graphite capsules) investigated the melting behaviour of a model amphibole-olivine-clinopyroxene rock, to assess the possible role of such cumulates in island arc magma genesis. Initial melts are controlled by pargasitic amphibole breakdown, are strongly nepheline-normative and are Al₂O₃-rich. With increasing melt fraction (T > 1190°C at 1.0 GPa), the melts become ultra-calcic while remaining strongly nepheline-normative, and are saturated with olivine and clinopyroxene. The experimental melts have strong compositional similarities to natural nepheline-normative ultra-calcic melt inclusions and lavas exclusively found in arc settings. The experimentally derived phase relations show that such natural melt compositions originate by melting according to the reaction amphibole + clinopyroxene = melt + olivine in the arc crust. Pargasitic amphibole is the key phase in this process, as it lowers melting temperatures and imposes the nepheline-normative signature. Ultra-calcic nepheline-normative melt inclusions are tracers of magma-rock interaction (assimilative recycling) in the arc crust.

KEY WORDS: *experimental melting; subduction zone; ultra-calcic melts; wehrlite*

INTRODUCTION

In subduction zones, the differentiation from high-MgO basalts to common andesitic lavas by fractional crystallization under H₂O-rich conditions begins with the generation of ultramafic cumulates (e.g. Kay & Kay, 1985; Himmelberg & Loney, 1995; Schiano *et al.*, 2004), which are probably ubiquitous at the base of the arc crust. The effect of water, as present in subduction zone primary magmas (Stolper & Newman, 1994; Sobolev & Chaussidon, 1996), is to expand the primary phase volumes of olivine, pyroxenes, and amphibole and shrink the stability field of plagioclase (e.g. Kushiro, 1969, 1974). At conditions typical for the basis of arc crust (near 1.0 GPa), the crystallization sequence is thus olivine → clinopyroxene → magnetite → amphibole → plagioclase (e.g. Holloway & Burnham, 1972; Helz, 1973), promoting the genesis of abundant plagioclase-free ultramafic cumulates. These cumulates are exposed in many arc roots, namely the 'Alaskan-type ultramafic-mafic intrusions' (Taylor 1967; Irvine, 1974; Clark, 1980; Snoke *et al.*, 1981; Andrew *et al.*, 1995; Himmelberg & Loney, 1995). Ultramafic olivine + clinopyroxene ± amphibole complexes have also been sampled as xenoliths by primitive arc basalts (e.g. Aoki, 1971; Arculus, 1978; Arculus & Wills, 1980; Conrad & Kay, 1984; Richard, 1986; Debari *et al.*, 1987; Turner *et al.*, 2003). Estimates based on crustal structures and compositions of

*Corresponding author. Present address: Department of Earth, Atmospheric, and Planetary Sciences, Massachusetts Institute of Technology, 77 Massachusetts Avenue, Building 54-1212, Cambridge, MA 02139, USA. Telephone: (1) 617 253 2876. Fax: (1) 617 253 7102. E-mail: emedard@mit.edu

island arcs may even suggest the existence of a 3–30 km ultramafic layer at the crust–mantle boundary, i.e. up to 50% of the island arc crust (Kay & Kay, 1985; Kushiro, 1990).

Most arc lavas are highly evolved and magmatic processes beneath island arc volcanoes involve crystallization, mixing and assimilation. In such a complex evolution, the study of melt inclusions in phenocrysts or xenocrysts (e.g. Schiano, 2003) yields information on intermediate steps in the evolution of the host magma and provides a window into magma generation processes, including partial melting, differentiation, mixing, and melt–wall-rock interactions. The investigation of melt inclusions in some high-Mg arc basalts (Schiano *et al.*, 2000, and references therein; de Hoog *et al.*, 2001) has shown that melt inclusions in the most magnesian olivine phenocrysts are not always primitive basalts. Rather, they bear a distinct population of ultra-calcic, nepheline-normative melt inclusions; similar compositions are also recorded in some island arc lavas. These ultra-calcic nepheline-normative melt inclusions have distinctive chemical compositions (Schiano *et al.*, 2000), in particular high CaO contents (up to 18.9 wt %), CaO/Al₂O₃ ratios (up to 1.25), and low SiO₂ contents (down to 44.0 wt %), rendering them nepheline-normative (up to 12% Ne in the CIPW norm). Other major element characteristics of these melt inclusions include relatively high MgO (up to 9.6 wt %) and highly variable FeO contents (5.7–12.3 wt %). Their trace element patterns are, however, typical of subduction-related magmas. Nepheline-normative ultra-calcic melt inclusions have been trapped in the most magnesian olivine phenocrysts, indicating an early formation in the history of the host magma. Schiano *et al.* (2000) argued that such ultra-calcic, nepheline-normative, melts cannot be formed from partial melting of common lherzolitic mantle as they strongly contrast with experimental melts of lherzolites under anhydrous or hydrous conditions (e.g. Falloon & Green, 1987; Baker & Stolper, 1994; Hirose & Kawamoto, 1995; Fig. 1). The origin of these ultra-calcic melt inclusions has thus been attributed to partial melting or melt–rock interaction involving olivine + clinopyroxene ± amphibole (Schiano *et al.*, 2000; Médard *et al.*, 2004). Hypersthene-normative ultra-calcic lavas, which have also been described from some arc settings (e.g. Barsdell & Berry, 1990), have very different characteristics and have been shown to originate by different mechanisms (Kogiso & Hirschmann, 2001; Médard *et al.*, 2004; Schmidt *et al.*, 2004), and thus will not be discussed further.

The aim of this study is thus to experimentally investigate the melting conditions and melt compositions of olivine + clinopyroxene + amphibole assemblages (thereafter referred to as ‘amphibole wehrlites’), commonly found as arc cumulates. The presence of amphibole is essential as amphibole lowers the melting

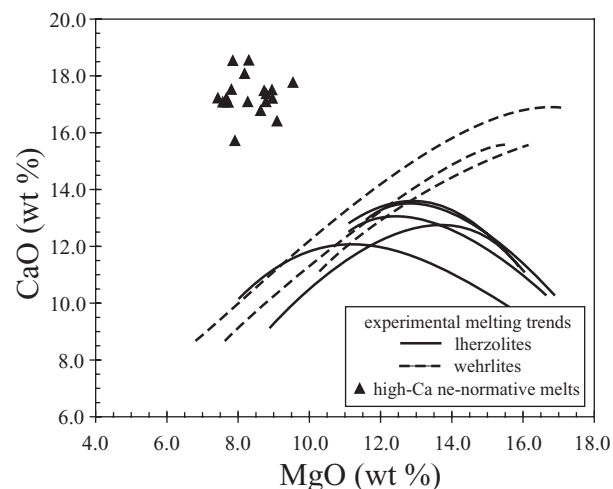


Fig. 1. Experimental melting trends for lherzolites (olivine + orthopyroxene + clinopyroxene ± spinel) and wehrlites (olivine + clinopyroxene) at 1.0 GPa, interpolated from the data of Falloon & Green (1987), Hirose & Kushiro (1993), Baker & Stolper (1994), Falloon *et al.* (2001), Kogiso & Hirschmann (2001), Schwab & Johnston (2001), Wasylenki *et al.* (2003), and Laporte *et al.* (2004). Wehrlite melting produces higher CaO content than lherzolite melting, but only at high MgO concentrations (i.e. high temperatures and high melt fractions). Nepheline-normative ultra-calcic melts from arc settings (Della-Pasqua & Varne, 1997; Schiano *et al.*, 2000; de Hoog *et al.*, 2001) cannot be explained by melting of lherzolites or wehrlites.

temperature (compared with dry melting) to $\sim 1100^{\circ}\text{C}$ (e.g. Holloway, 1972; Niida & Green, 1999). Metasomatic amphibole wehrlites have also been documented in island arcs (Richard, 1986) and intraplate settings (e.g. O'Reilly & Griffin, 1988); their melting behaviour should not significantly differ from that of cumulative amphibole wehrlites.

EXPERIMENTAL AND ANALYTICAL PROCEDURES

Choice of starting material

Representative mineral compositions in cumulative amphibole–clinopyroxene–olivine rocks are given in Table 1. The most prominent features are the low X_{Mg} [$X_{\text{Mg}} = \text{Mg}/(\text{Mg} + \text{Fe}^{\text{tot}})$] of olivine (0.733–0.865) and high CaO (>21.0%), low Al₂O₃ (<6.1%) and Na₂O (<0.4%) contents of clinopyroxene. Low X_{Mg} olivine is characteristic of olivine-poor cumulates; however, some associated dunites contain olivines with X_{Mg} up to 0.949 (Himmelberg & Loney, 1995). Amphiboles are typically pargasites to pargasitic hornblendes; as a consequence of their low SiO₂ and high Na₂O contents, they are nepheline-normative. This is a characteristic feature of amphiboles crystallizing from basaltic or low-silica andesitic compositions (e.g. Holloway & Burnham, 1972; Helz, 1973; Gill, 1981).

Table 1: Phase proportions and compositions in representative olivine–clinopyroxene–amphibole cumulates from arc settings

	M102	2215	80BI14	SA24	OCA2
<i>Phase proportions (wt %)</i>					
olivine	20	33	9		19
cpx	28	33	80	85	45
hbl	52	33	11	15	36
<i>Olivine</i>					
Mg-no.	86.6	83.0	80.4		80.7
<i>Clinopyroxene</i>					
SiO ₂	52.16	49.53	52.26	50.61	50.29
TiO ₂	0.21	0.61	0.26	0.57	0.62
Al ₂ O ₃	3.64	4.91	2.87	5.15	4.35
Cr ₂ O ₃	0.99	n.d.	0.23	n.d.	0.14
FeO*	3.70	6.94	4.41	6.50	6.38
MgO	16.47	14.48	15.99	14.14	14.29
CaO	22.51	23.11	23.68	22.73	23.49
Na ₂ O	0.24	0.21	0.18	0.30	0.27
Mg-no.	88.6	78.4	86.3	79.5	79.6
<i>Amphibole (pargasite)</i>					
SiO ₂	42.10	41.74	45.27	41.30	41.27
TiO ₂	1.18	1.56	1.00	1.72	1.77
Al ₂ O ₃	15.09	14.38	12.24	14.39	14.38
Cr ₂ O ₃	0.44	n.d.	n.d.	n.d.	n.d.
FeO*	6.98	9.77	8.49	10.32	9.64
MgO	16.44	15.48	16.26	14.50	14.93
CaO	12.55	12.17	12.55	11.91	12.63
Na ₂ O	2.65	2.04	1.59	2.22	1.97
K ₂ O	0.60	0.74	0.50	1.66	1.31
Mg-no.	80.8	73.8	77.3	71.5	73.4

M102, Mount Adagdak xenolith, Adak Island, Alaska (Conrad & Kay, 1984); 2215, Itinomegata ultramafic xenolith, Japan (Aoki, 1971); 80BI14, amphibole–olivine clinopyroxenite in Blashke Island Alaskan-type complex (Himmelberg & Loney, 1995); SA24, Sangeang Api xenolith, Sunda arc (Turner *et al.*, 2003); OCA2, average mineral compositions in Alaskan-type complexes (from Himmelberg & Loney, 1995). Clinopyroxenes analyses have been recalculated to 100%, and amphiboles to 98%, to facilitate comparison.

Phase proportions in cumulate rocks are highly variable. Alaskan-type arc cumulates vary from dunites to clinopyroxenites to hornblendites (Debari *et al.*, 1987; Himmelberg & Loney, 1995), containing various proportion of olivine, clinopyroxene and amphibole, with often minor spinel phases (chromite, magnetite or aluminous spinel). For this study, phase proportions were

Table 2: Starting material and whole-rock compositions of natural cumulates (wt %, recalculated to 100% anhydrous)

	Starting	Natural		
	OCA2	M102	80BI14	SA24
Olivine:	19	20	9	
Cpx:	45	28	80	85
Amphibole:	36	52	11	15
SiO ₂	45.5 (4)	44.55	48.60	48.84
TiO ₂	1.18 (08)	0.67	0.31	0.71
Al ₂ O ₃	7.4 (3)	8.87	3.66	6.11
Cr ₂ O ₃	0.09 (05)	0.51		
FeO*	9.5 (6)	7.24	7.56	7.05
MgO	19.9 (4)	22.52	18.00	14.08
CaO	15.0 (3)	12.83	20.10	21.11
Na ₂ O	0.90 (11)	1.45	0.22	0.58
K ₂ O	0.43 (02)	0.31	0.00	0.40
X _{Mg}	0.789	0.847	0.809	0.781
CaO/Al ₂ O ₃	2.02	1.45	5.49	3.46

Natural cumulate compositions from Conrad & Kay (1984), Himmelberg & Loney (1995) and Turner *et al.* (2003). The numbers in parentheses are 2σ standard deviations, given in terms of the last unit cited. OCA2 is the experimental starting composition.

chosen to optimize the experimental melt fraction, while maintaining saturation in clinopyroxene and olivine: the synthetic starting material, OCA2, was calculated as a mix of 45 wt % clinopyroxene, 36 wt % amphibole and 19 wt % olivine. Cumulates with similar phase proportions (Table 1) have been found, for example, at Batan volcano, in the Philippines (Richard, 1986) and Itinomegata, in Japan (Aoki, 1971). As long as the partial melts remain saturated with olivine, removing olivine from the source will only change the Mg/Fe systematic of the melts (Green & Ringwood, 1970; Jaques & Green, 1980). The experiments are, thus, directly relevant to melting of dunites with minor interstitial amphibole and clinopyroxene, as well as melting of clinopyroxene–amphibole rocks with minor olivine. Olivine-free clinopyroxene–amphibole rocks that generate olivine by incongruent amphibole melting are also approximated by this study. For simplification purposes, all these amphibole + clinopyroxene ± olivine rocks with similar melting behaviour will be referred to hereafter as ‘amphibole wehrlites’ (although the OCA2 starting material, for example, is nominally an olivine–amphibole clinopyroxenite).

Table 3: Summary of experimental conditions, and calculated phase proportions (wt %)

Run no.	<i>P</i> (GPa)	<i>T</i> (°C)	<i>t</i> (h)	pyr*	vcs†	glass	cpx	olivine	<i>r</i> ²
wh31	1.0	1350	6.0	×		0.772 (30)	0.056 (11)	0.172 (30)	0.02
wh17	1.0	1350	6.0			0.775 (31)	0.044 (14)	0.181 (29)	0.07
wh18	1.0	1325	9.0			0.661 (31)	0.141 (15)	0.199 (30)	0.02
wh33	1.0	1300	12.0	×	×	0.628 (27)	0.176 (11)	0.196 (29)	0.01
wh20	1.0	1300	11.5		×	0.558 (27)	0.231 (13)	0.211 (25)	0.03
wh08	1.0	1300	55.1			0.350 (22)	0.409 (12)	0.241 (20)	0.13
wh19	1.0	1275	24.9		×	0.453 (25)	0.319 (13)	0.228 (24)	0.05
wh21	1.0	1250	24.0		×	0.328 (28)	0.431 (14)	0.241 (27)	0.13
wh24	1.0	1225	47.3	×	×	0.434 (29)	0.337 (12)	0.229 (29)	0.07
wh27	1.0	1225	49.9	×	×	0.393 (23)	0.376 (10)	0.231 (25)	0.18
wh39	1.0	1225	24.0	×	×	0.205 (20)	0.535 (11)	0.260 (23)	0.36
wh07	1.0	1200	72.3		×	0.256 (26)	0.491 (12)	0.253 (27)	0.21
wh40	0.5	1300	6.0	×	×	0.755 (28)	0.045 (12)	0.200 (29)	0.01
wh14	0.5	1260	60.0		×	0.496 (19)	0.262 (10)	0.242 (22)	0.04
wh26	0.5	1250	24.0	×	×	0.442 (21)	0.313 (10)	0.245 (22)	0.51
wh28	0.5	1200	48.0	×	×	0.185 (13)	0.536 (10)	0.278 (17)	0.04
wh15	0.5	1175	60.0		×	0.230 (14)	0.495 (11)	0.275 (18)	0.31
wh44	0.5	1175	10.5		×	0.233 (17)	0.490 (13)	0.277 (21)	0.38

All experiments were performed in single-stage piston-cylinders, with the exception of wh14 and wh15, which were performed in an internally heated pressure vessel. *r*² is the sum of weighted squared residual from phase proportions calculation.

*pyr refers to assemblages with an ~200 mg sleeve of unfired pyrophyllite around the capsule.

†vcs indicates the experiments where 15–30% vitreous carbon spheres were placed at the hot end of the charge.

Preparation of starting material

Average mineral compositions from Alaskan-type cumulates were chosen as representative for arc crustal cumulates (Table 1). The OCA2 starting material (Table 2) has been obtained from mixing analytical grade oxides (SiO₂, TiO₂, Al₂O₃, Cr₂O₃, Fe₂O₃, MgO), synthetic feldspars, diopside, and fayalite. Water (1.0 wt %) was introduced into the mix in the form of Al(OH)₃; this is slightly higher than the 0.8 wt % required by amphibole proportions, and is intended to partially compensate for water losses during the experiments. The Fe³⁺/Fe^{total} ratio was set to 0.2; in fresh cumulates from Batan Island and Itinomegata, Fe³⁺/Fe^{total} ratios were 0.15 and 0.35, respectively (Aoki, 1971; Richard, 1986). The starting material was ground under ethanol to ≤10 μm and dried for at least 6 h at 110°C before loading. A small portion of the powder was formed into a 2 mm diameter pellet, placed on a platinum wire loop pre-equilibrated (by a prior melting step) with the starting material and fused for 2 min at 1550°C in a 1 atm CO₂–H₂ gas-mixing quench furnace, with *f*O₂ = QFM (quartz–fayalite–magnetite buffer). Longer run times resulted in losses of alkalis. The resulting homogeneous brown glass was analysed by electron microprobe (Table 2).

Experimental methods

Most partial melting experiments at 0.5 and 1.0 GPa (Table 3) were performed in single-stage piston-cylinders at the Laboratoire Magmas et Volcans. A 12.7 mm diameter bore was used at 1 GPa and a 19.1 mm diameter bore at 0.5 GPa. Double capsules composed of an inner graphite container and an outer platinum capsule were employed (1.0 mm i.d. graphite, 2.6 mm i.d. Pt, 3.0 mm o.d. Pt). Platinum capsules were welded while cooled by water to avoid dehydration of Al(OH)₃ and checked for leaks by weighing after 1 h in an acetone bath. For some experiments, the capsules were encased in a 100–200 mg pyrophyllite sleeve, to reduce hydrogen fugacity gradients between assembly and sample, and thus water losses (Freda *et al.*, 2001). Our assemblies comprised a NaCl cell wrapped in lead foil, an outer Pyrex sleeve, a graphite furnace, an inner Pyrex sleeve (only for the 19.1 mm assembly) and inner rods of crushable MgO. Temperature was measured using a W₇₄Re₂₆–W₉₅Re₅ thermocouple and maintained within 1°C of the setpoint. The temperature difference over the capsule length was previously measured to ~15°C or less at 1100–1300°C. For our low-friction lead–NaCl assemblies, a pressure correction was found to be unnecessary

(Boettcher *et al.*, 1981), and the uncertainty on the nominal pressure is assumed to be 0.05 GPa at 1.0 GPa, and 0.1 GPa at 0.5 GPa. Two 0.5 GPa experiments (wh14 and wh15) were performed in an internally heated pressure vessel, using the same capsule configuration. Temperature was measured using a Pt₉₀Rh₁₀–Pt₇₀Rh₃₀ thermocouple; temperature gradients are negligible and the temperature accuracy is thought to be within $\pm 5^\circ\text{C}$. Pressure uncertainties do not exceed 5 MPa.

The presence of graphite in high-pressure experiments delimits oxygen fugacities ($f\text{O}_2$) to maximum values of the graphite–CO buffer. $f\text{O}_2$ values in similar experiments (Médard *et al.*, 2004; Schmidt *et al.*, 2004) have been estimated to be about QFM – 2, QFM – 3 [QFM from O'Neill (1987)], which is probably lower than oxygen fugacities in subduction zone magmas (e.g. Parkinson & Arculus, 1999). Experiments performed by Schmidt *et al.* (2004), using Pt–graphite capsules and more oxidizing AuPd capsules, show that varying $f\text{O}_2$ would only affect the iron content of the melts, the stability of Fe³⁺-rich spinel, and marginally affect the melting temperatures ($\sim 10^\circ\text{C}$). The consequences of these variations will be detailed in the discussion section. The presence of ferric iron and water in the starting material might result in some dissolved CO₂, which for our experimental melts was estimated to a maximum of 0.4–1.0 wt % in the lowest melt fraction experiments (0.4–1.0% = 100% – electron microprobe totals – H₂O concentration by ion probe). At low pressure, low CO₂ solubility will have a fairly small effect on phase relations and melting temperatures, as can be seen in Wendlandt & Mysen (1980), Tatsumi *et al.* (1999) or Schmidt *et al.* (2004) experiments.

Melt segregation techniques

Despite the high quench rate of the piston-cylinder apparatus (up to 175°C/s in our 12.7 mm assembly), the presence of water results in strong quench-modifications, requiring efficient segregation of the partial melts. Melt segregation was obtained by taking advantage of the thermal gradient in the capsule and by the use of a vitreous carbon sphere layer as a melt trap.

Any thermal gradient in experimental charges promotes dissolution–precipitation that works towards partial segregation of the melt into the hotspot of the experimental charge. This thermal migration mechanism (Leshner & Walker, 1988) has already been successfully used for driving melt segregation in multi-anvil experiments (e.g. Walter, 1998). To obtain an efficient segregation, a layer of vitreous carbon spheres 20–50 µm in diameter was placed at the base (corresponding to the hot zone) of most experimental charges (Fig. 2 and Table 3; Wasylenki *et al.*, 1996). This layer constituted 15–30% of the total volume of the sample. Available pore space is estimated at $\leq 50\%$ of the carbon sphere layer, a porosity

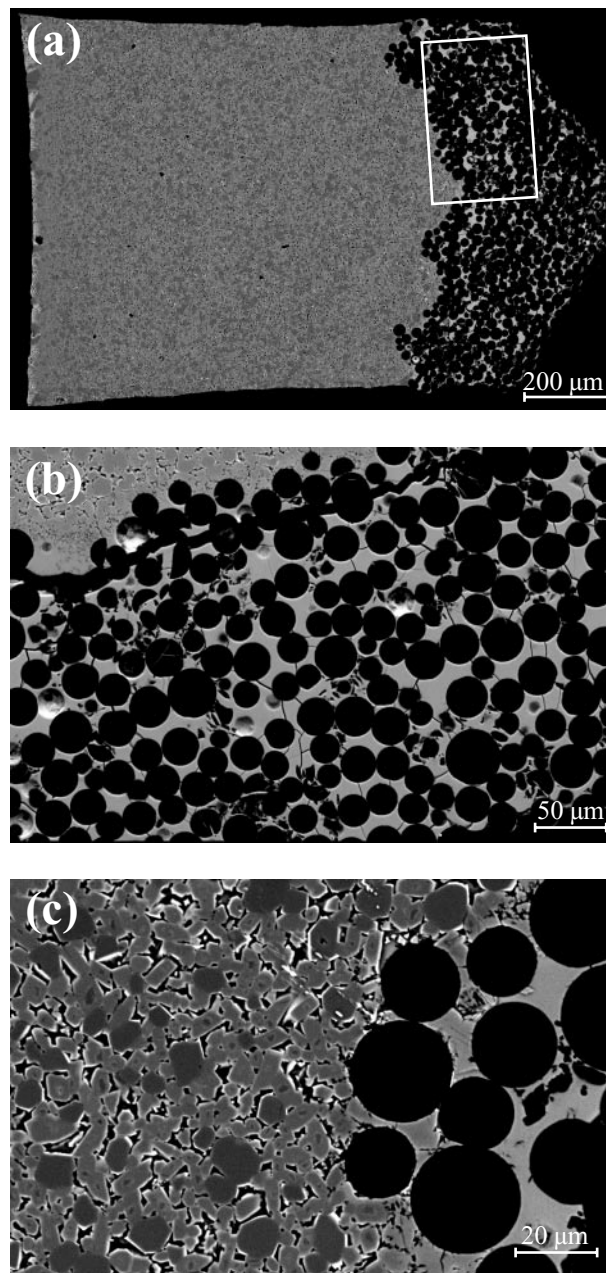


Fig. 2. Backscattered electron images illustrating the experimental melt extraction technique. (a) Charge with vitreous carbon sphere layer at the bottom (right part in the image); (b) a detail of the same charge showing the vitreous carbon spheres (black) surrounded by glass (grey). The melt is isolated from the equilibrium crystals (upper left corner); (c) a closer view that shows some quench crystals at the interface between carbon spheres + glass and residual crystals + glass layers. Crystals are absent in the sphere layer beyond 20–30 µm from the interface. Experiment wh26 at 0.5 GPa, 1250°C and 44% melt.

always completely filled by the melt fraction (> 15 wt %); ‘excess’ interstitial melt is present in all experimental charges. This melt extraction technique has been discussed further by Wasylenki *et al.* (2003, and references

therein). In the low-temperature experiments at 1.0 GPa, which are also the longest and those with the highest initial H₂O concentrations in the melt, vitreous carbon begins to devitrify, and small graphite needles crystallize in the interstitial melts. In the three lowest-temperature experiments at 1.0 GPa (wh07, wh21, wh29; Table 3), these graphite needles favoured clinopyroxene nucleation during quench, and glasses could not be analysed. However, area scan analyses of melt + quench clinopyroxenes + carbon spheres give an approximation of equilibrium melt compositions.

The only compositional zoning through the charge consists of a slight variation in X_{Mg} of olivine crystals (X_{Mg} variations are in the range 1–3 σ in term of analytical errors). Equilibrium values of crystals were obtained by systematically analysing solid phases in direct contact with the segregated melt, i.e. near the hotspot at the base of the charge.

Analytical methods

Compositions of crystalline phases and glasses were determined with a Cameca SX100 electron microprobe at Clermont-Ferrand. For crystalline phases, beam conditions of 15 kV and 15 nA were employed, counting times were 10 s and the electron beam was focused. For glass analyses, the beam current was 8 nA and the beam spread to 10 μm . In the three experiments where the melt quenched to a mixture of glass and quench clinopyroxene, we estimated melt composition by performing broad area scans. Areas of varying size were analysed; major element compositions remained constant from 20 $\mu\text{m} \times 20 \mu\text{m}$ to 50 $\mu\text{m} \times 50 \mu\text{m}$.

Water concentrations in some glasses were determined using the Cameca IMS 4f ion microprobe at Pavia, following a procedure similar to that described by Ottolini *et al.* (1995, 2002). A $^{16}\text{O}^-$ primary ion beam of 2.6–3.0 nA current intensity was used to sputter the samples, corresponding to a beam spot of <10 μm . Secondary positive ions, $^1\text{H}^+$ and $^{30}\text{Si}^+$, were monitored in the energy range of 75–125 eV. Counting times were 30 s for $^1\text{H}^+$ and 20 s for $^{30}\text{Si}^+$ over five cycles. Measurements were made under steady-state sputtering conditions achieved after 660 s of sputtering. To reduce adsorbed water, samples were left to degas overnight in the ion microprobe sample chamber together with the standards. DL-5 (CNR-IGG reference amphibole) was used as the primary standard for H in the calibration of the H^+ and Si^+ ion signals. The relative-to-Si ion yield for H was tested on another reference amphibole Z2081, and agrees within uncertainty with those obtained on two basaltic standards (CLDR01-5V and CY82-29-1V, Ottolini *et al.*, 1995). The samples were corrected for background using an anhydrous garnet standard. Two to four spots were analysed on each sample; the uncertainty on the

determined H₂O content is estimated to be of the order of 15% relative.

For samples that could not be analysed for H₂O because of the small size of their glass pools, the H₂O contents were estimated using a ‘by-difference’ method modified after Devine *et al.* (1995). The difference to 100% of electron microprobe analyses was calibrated against the H₂O contents of glasses analysed by ion microprobe. Using standards from the same experimental series allows avoidance of any matrix effect in the microprobe analyses, and introduction of a correction for the small amounts of CO₂ that might be present in the experiments. These standard glasses were analysed together with the experimental glasses during each microprobe session. The error on H₂O contents obtained through the ‘by-difference’ method is estimated at ~25% relative (Médard, 2004).

RESULTS

Experimental results are summarized in Table 3 (experimental conditions) and Tables 4–6 (phase compositions). All experiments contain clinopyroxene, olivine and glass; amphibole is never present, as the experiments were performed at temperatures exceeding pargasite stability (which is situated near 1100°C at 1.0 GPa, Holloway, 1972).

Attainment of equilibrium

Run durations varied from 60 to 6 h, decreasing with increasing melt fraction (and temperature). Two minerals were present both in the starting material (diopside and fayalite) and run products (clinopyroxene and olivine). Olivine crystals were unzoned; however, residual Ca- and Mg-rich clinopyroxene cores <2 μm in diameter were observed in the lowest temperature experiments. The use of diopside as a starting material proved to be a strategic error: clinopyroxene crystals have very low diffusional equilibration rates (Cherniak, 2001), and clinopyroxenes in partial melting experiments maintain unreacted cores, which persist almost indefinitely (e.g. Baker & Stolper, 1994; Pickering-Witter & Johnston, 2000). In some low-temperature experiments, clinopyroxenes have diopside cores and quench rims, making it difficult to obtain good analyses of the intermediate equilibrated zones. In the low-temperature experiments, clinopyroxene analyses were thus carefully sorted to exclude quench-related (high Ca-Tschermaks component) and residual core compositions (nearly pure diopside); the low sums of squared residuals in mass balance calculations indicate that the selected compositions are close to equilibrium.

Equilibration of our oxide-mix–mineral starting material was tested at the lowest temperature conditions.

Table 4: Average composition¹ (wt %) of melts from OCA2 olivine–clinopyroxene–amphibole cumulate composition

Run:	wh31	wh17	wh18	wh33	wh20	wh08	wh19	wh24	wh27
<i>P</i> (GPa):	1.0	1.0	1.0	1.0	1.0	1.0	1.0	1.0	1.0
<i>T</i> (°C):	1350	1350	1325	1300	1300	1300	1275	1225	1225
<i>F</i> (%):	0.772	0.775	0.661	0.628	0.558	0.350	0.453	0.434	0.393
<i>n</i> :	19	29	9	12	10	5	14	7	13
SiO ₂	46.2 (4)	46.2 (5)	45.3 (6)	45.3 (6)	44.8 (7)	43.9 (4)	44.3 (5)	44.1 (4)	44.4 (6)
TiO ₂	1.50 (18)	1.43 (24)	1.66 (17)	1.6 (4)	1.73 (14)	2.03 (24)	2.03 (17)	2.08 (17)	2.11 (15)
Al ₂ O ₃	9.46 (27)	9.44 (31)	10.7 (3)	10.9 (2)	11.8 (3)	13.8 (4)	12.9 (3)	13.3 (5)	14.0 (3)
FeO*	9.72 (33)	9.50 (28)	10.2 (4)	10.5 (5)	10.8 (2)	11.8 (3)	11.2 (4)	11.5 (5)	11.5 (5)
MgO	13.8 (4)	13.6 (6)	12.5 (5)	12.3 (4)	11.5 (1)	9.29 (15)	10.3 (3)	10.2 (3)	9.69 (22)
CaO	17.6 (4)	17.8 (4)	17.6 (5)	17.2 (4)	17.0 (2)	15.6 (2)	16.3 (4)	16.1 (5)	15.3 (6)
Na ₂ O	1.16 (11)	1.33 (9)	1.34 (19)	1.36 (16)	1.55 (15)	2.42 (6)	1.90 (24)	1.80 (24)	1.95 (26)
K ₂ O	0.55 (10)	0.53 (20)	0.63 (8)	0.65 (9)	0.76 (15)	1.10 (11)	0.88 (12)	0.93 (14)	1.01 (12)
Sum ²	97.92	98.34	97.60	97.28	97.83	98.80	97.24	96.25	96.08
H ₂ O	1.22	0.75	1.01	1.26	0.72	0.05	0.95 ³	2.11 ³	1.65 ³
H ₂ O _{bulk} ⁴	0.94	0.58	0.67	0.79	0.40	0.02	0.43	0.92	0.65
X _{Mg}	0.716	0.719	0.687	0.675	0.655	0.583	0.621	0.613	0.600
CaO/Al ₂ O ₃	1.86	1.89	1.66	1.57	1.44	1.13	1.26	1.21	1.09
ne ⁵	5.3	6.1	6.2	6.2	7.1	11.1	8.7	8.3	9.0
Run:	wh21	wh39	wh07	wh40	wh14	wh26	wh28	wh15	wh44
<i>P</i> (GPa):	1.0	1.0	1.0	0.5	0.5	0.5	0.5	0.5	0.5
<i>T</i> (°C):	1250	1225	1200	1300	1260	1250	1200	1175	1175
<i>F</i> (%):	0.328	0.205	0.256	0.755	0.496	0.442	0.185	0.230	0.233
<i>n</i> :	18	10	10	11	16	10	11	12	10
SiO ₂	44.5 (11)	45.5 (13)	44.4 (7)	46.5 (7)	44.5 (6)	45.2 (8)	46.3 (6)	44.0 (5)	44.6 (5)
TiO ₂	2.0 (4)	1.8 (5)	2.1 (3)	1.55 (19)	1.91 (21)	1.93 (19)	1.80 (21)	2.07 (26)	2.07 (10)
Al ₂ O ₃	14.4 (4)	16.7 (6)	15.2 (5)	9.72 (25)	13.2 (3)	14.2 (4)	18.7 (3)	17.8 (4)	17.5 (4)
FeO*	11.7 (8)	10.6 (6)	11.7 (6)	9.52 (27)	10.6 (4)	10.6 (4)	9.49 (36)	11.0 (6)	10.8 (3)
MgO	8.93 (40)	7.15 (43)	8.33 (52)	12.6 (5)	9.62 (39)	8.87 (32)	5.46 (26)	6.17 (34)	6.04 (34)
CaO	14.6 (7)	12.4 (8)	13.5 (6)	18.2 (4)	17.2 (5)	16.2 (5)	11.8 (4)	13.3 (7)	13.6 (4)
Na ₂ O	2.50 (38)	3.35 (54)	2.51 (42)	1.20 (18)	2.03 (23)	2.07 (07)	4.18 (47)	3.86 (47)	3.55 (42)
K ₂ O	1.26 (35)	2.42 (42)	2.11 (23)	0.56 (08)	0.89 (08)	1.00 (14)	2.24 (16)	1.80 (13)	1.87 (16)
Sum ²	57.18 ⁶	45.85 ⁶	38.84 ⁶	97.92	97.71	97.50	98.19	97.81	97.27
H ₂ O				1.13	0.23 ³	1.10 ³	0.84 ³	0.76 ³	1.01 ³
H ₂ O _{bulk} ⁴				0.85	0.11	0.49	0.16	0.17	0.24
X _{Mg}	0.576	0.545	0.559	0.703	0.619	0.599	0.506	0.500	0.499
CaO/Al ₂ O ₃	1.02	0.74	0.89	1.88	1.30	1.14	0.63	0.75	0.77
ne ⁵	11.44	15.34	11.49	5.49	9.30	9.50	18.58	17.67	16.26

¹The numbers in parentheses are 2σ standard deviations, given in terms of the last unit cited.

²Analyses have been recalculated to 100% anhydrous; the 'sum' row corresponds to the original analytical total.

³H₂O concentrations estimated with the by-difference method; other H₂O concentrations were measured by ion microprobe at CNR-IGG (Pavia).

⁴Bulk H₂O contents, calculated from melt H₂O concentrations and melt fraction.

⁵Normative nepheline content (Cross *et al.*, 1903), calculated assuming all Fe is Fe²⁺.

⁶Former melt compositions estimated from broad scan analyses of 20 μm × 20 μm to 50 μm × 50 μm areas containing glass, quench clinopyroxenes and vitreous carbon spheres. The difference between the analytical totals and 100% represents C from the carbon spheres.

n, number of analyses.

Table 5: Average composition¹ of olivines in partial melting experiments on OCA2 starting material

Run:	wh31	wh17	wh18	wh33	wh20	wh08	wh19	wh24	wh27
<i>P</i> (GPa):	1	1	1	1	1	1	1	1	1
<i>T</i> (°C):	1350	1350	1325	1300	1300	1300	1275	1225	1225
<i>n</i> :	10	9	6	10	5	4	8	7	10
SiO ₂	40.2 (5)	40.7 (5)	40.3 (5)	39.8 (6)	40.5 (5)	39.7 (8)	40.1 (6)	40.2 (6)	39.8 (8)
FeO*	10.5 (3)	10.2 (2)	11.8 (3)	12.2 (4)	12.7 (3)	15.6 (2)	14.1 (3)	14.5 (2)	15.4 (3)
MgO	48.5 (4)	48.2 (6)	47.0 (6)	47.1 (5)	45.8 (5)	43.7 (6)	45.0 (6)	44.6 (8)	44.1 (6)
CaO	0.71 (10)	0.76 (11)	0.75 (10)	0.73 (23)	0.82 (10)	0.80 (5)	0.73 (12)	0.60 (9)	0.57 (12)
Sum ²	101.34	99.93	100.23	101.05	100.48	101.25	100.98	100.42	100.55
<i>X</i> _{Mg} ³	0.892 (4)	0.893 (3)	0.877 (4)	0.873 (5)	0.865 (4)	0.833 (4)	0.851 (4)	0.846 (4)	0.836 (4)
<i>K</i> _{d ol/liq} ³	0.31 (3)	0.31 (3)	0.31 (3)	0.30 (3)	0.30 (2)	0.28 (2)	0.29 (3)	0.29 (3)	0.29 (3)
Run:	wh21	wh39	wh07	wh40	wh14	wh26	wh28	wh15	wh44
<i>P</i> (GPa):	1.0	1.0	1.0	0.5	0.5	0.5	0.5	0.5	0.5
<i>T</i> (°C):	1250	1225	1200	1300	1260	1250	1200	1175	1175
<i>n</i> :	6	6	5	5	6	6	5	9	5
SiO ₂	39.7 (8)	39.4 (6)	39.3 (6)	40.0 (7)	40.1 (2)	39.7 (7)	38.7 (9)	39.5 (6)	38.7 (8)
FeO*	15.6 (4)	17.8 (4)	17.3 (3)	10.8 (3)	13.9 (2)	15.0 (3)	19.5 (5)	18.5 (3)	18.8 (3)
MgO	43.8 (8)	42.0 (6)	42.7 (5)	48.3 (6)	44.9 (2)	44.2 (5)	40.9 (8)	41.1 (6)	41.6 (7)
CaO	0.72 (15)	0.62 (18)	0.67 (12)	0.79 (9)	0.87 (16)	0.87 (21)	0.65 (17)	0.79 (15)	0.78 (4)
Sum ²	100.76	99.56	101.20	100.93	98.94	99.76	98.88	99.37	97.41
<i>X</i> _{Mg} ³	0.834 (6)	0.808 (6)	0.815 (4)	0.889 (4)	0.852 (2)	0.840 (5)	0.789 (7)	0.798 (5)	0.798 (5)
<i>K</i> _{d ol/melt} ³	0.27 (4)	0.28 (4)	0.29 (4)	0.30 (3)	0.28 (3)	0.29 (3)	0.27 (4)	0.25 (4)	0.25 (3)

¹The numbers in parentheses are 2σ standard deviations, given in terms of the last unit cited.

²Analyses have been recalculated to 100% anhydrous, the ‘sum’ row corresponds to the original analytical total.

³*X*_{Mg} and olivine–melt *K*_d calculated assuming all Fe as FeO.

TiO₂, Al₂O₃, Cr₂O₃, Na₂O, K₂O are below detection limit. *n*, number of analyses.

At 0.5 GPa and 1175°C, 10.5 h and 60.0 h run times (runs wh15 and wh44), glasses have similar water contents and glass and mineral compositions are identical within error (Tables 4–6). The rapid equilibration is probably a consequence of the high melt fraction and the strongly depolymerized structure of the melt, enhanced by the presence of water in the partial melts, which increases diffusion rates.

Crystals show idiomorphic textures (Fig. 3), with the exception of some easily identifiable quench growth rims. To evaluate the degree of chemical equilibration, olivine–melt Fe–Mg distribution coefficients were calculated. These vary between 0.25 and 0.32, which is lower than or equal to the results of other experimental studies (e.g. Baker & Stolper, 1994; Falloon *et al.*, 2001; Kogiso & Hirschmann, 2001) giving values in the range 0.32 ± 0.02. The lowest *K*_d would be explained by a melt Fe^{III}/Fe^{total} ratio of 0.15. Glass analyses performed in the immediate vicinity of olivine or pyroxene crystals are modified by diffusion during quenching, MgO

being the most affected oxide. Analyses with low MgO contents (less than mean value – 2σ) have thus been excluded. In the charges in which broad area scans were necessary, *X*_{Mg} of the melt indicates equilibrium with olivine and clinopyroxene crystals, and melt compositions fall within oxide vs oxide trends defined by the other experiments (see Fig. 6). These results combined with low *r*² in mass balance calculations indicate that the melt compositions before quenching have been approximated correctly.

Control of the melt H₂O content

CaO and Al₂O₃ contents of the partial melts are well correlated with melt fraction and MgO content (Fig. 4). However, at low temperatures and long run durations, there is a relatively poor correlation between temperature and melt composition (Fig. 4), or temperature and melt fraction (Fig. 5), which is due to variable bulk water contents, resulting from variable water loss (probably by

Table 6: Average composition¹ of clinopyroxenes in partial melting experiments on OCA2 starting material

Run:	wh31	wh17	wh18	wh33	wh20	wh08	wh19	wh24	wh27
<i>P</i> (GPa):	1-0	1-0	1-0	1-0	1-0	1-0	1-0	1-0	1-0
<i>T</i> (°C):	1350	1350	1325	1300	1300	1300	1275	1225	1225
<i>n</i> :	6	6	6	7	7	5	5	6	7
SiO ₂	53.5 (7)	53.6 (4)	52.9 (6)	52.4 (6)	52.2 (11)	50.1 (5)	51.5 (6)	51.3 (14)	51.0 (10)
TiO ₂	0.39 (7)	0.42 (10)	0.50 (12)	0.57 (20)	0.65 (18)	1.12 (19)	0.79 (12)	0.77 (26)	0.84 (18)
Al ₂ O ₃	2.3 (6)	2.3 (6)	2.9 (9)	3.3 (9)	3.8 (11)	7.0 (9)	5.1 (8)	5.0 (16)	5.2 (8)
Cr ₂ O ₃	0.20 (6)	0.23 (8)	0.26 (29)	0.24 (7)	0.21 (23)	0.17 (10)	0.21 (14)	0.17 (14)	0.19 (5)
FeO*	2.98 (25)	2.85 (21)	3.18 (33)	3.37 (44)	3.45 (36)	3.82 (14)	3.61 (41)	3.96 (51)	4.00 (36)
MgO	17.8 (4)	17.4 (5)	16.9 (7)	17.0 (5)	16.4 (7)	14.8 (6)	15.6 (7)	15.4 (8)	15.4 (4)
CaO	22.7 (7)	23.1 (5)	23.1 (4)	23.0 (9)	23.0 (9)	22.7 (4)	23.0 (7)	23.2 (7)	23.0 (5)
Na ₂ O	0.16 (3)	0.14 (5)	0.18 (3)	0.21 (6)	0.22 (6)	0.32 (8)	0.29 (3)	0.28 (5)	0.28 (7)
Sum ²	101.05	99.83	100.52	100.65	100.45	100.34	100.48	100.88	100.60
X _{Mg} ³	0.914	0.916	0.904	0.900	0.895	0.873	0.885	0.874	0.873
Si	1.940	1.946	1.926	1.904	1.903	1.830	1.877	1.874	1.862
Ti	0.011	0.011	0.014	0.015	0.018	0.031	0.022	0.021	0.023
Al	0.097	0.098	0.124	0.139	0.163	0.302	0.218	0.213	0.226
Cr	0.006	0.007	0.008	0.007	0.006	0.005	0.006	0.005	0.005
Fe ²⁺	0.009	0.000	0.003	0.029	0.006	0.000	0.000	0.012	0.019
Fe ³⁺	0.081	0.087	0.094	0.073	0.099	0.117	0.110	0.109	0.103
Mg	0.964	0.944	0.916	0.922	0.891	0.805	0.848	0.839	0.839
Ca	0.882	0.898	0.902	0.894	0.899	0.887	0.898	0.907	0.901
Na	0.011	0.010	0.013	0.015	0.015	0.022	0.021	0.020	0.020
Run:	wh21	wh39	wh07	wh40	wh14	wh26	wh28	wh15	wh44
<i>P</i> (GPa):	1-0	1-0	1-0	0-5	0-5	0-5	0-5	0-5	0-5
<i>T</i> (°C):	1250	1225	1200	1300	1260	1250	1200	1175	1175
<i>n</i> :	6	4	8	5	6	6	4	5	3
SiO ₂	49.8 (12)	49.2 (10)	49.4 (13)	53.3 (2)	52.5 (5)	52.4 (6)	49.7 (2)	49.7 (4)	49.7 (8)
TiO ₂	1.04 (19)	1.22 (28)	1.24 (29)	0.42 (15)	0.64 (9)	0.66 (17)	1.30 (33)	1.33 (18)	1.30 (29)
Al ₂ O ₃	6.5 (9)	7.4 (6)	6.9 (11)	1.81 (31)	2.93 (21)	3.1 (8)	7.2 (14)	6.74 (23)	6.0 (7)
Cr ₂ O ₃	0.16 (5)	n.a.	n.a.	0.28 (31)	0.21 (11)	0.20 (17)	0.23 (23)	0.22 (27)	n.a.
FeO*	3.90 (41)	4.43 (28)	4.36 (20)	2.73 (57)	3.35 (27)	3.56 (14)	4.22 (64)	3.75 (32)	4.35 (14)
MgO	15.2 (4)	14.3 (4)	14.4 (5)	17.5 (1)	16.3 (2)	16.2 (4)	13.8 (15)	14.5 (3)	14.2 (7)
CaO	23.1 (5)	23.0 (2)	23.3 (6)	23.8 (9)	23.8 (4)	23.7 (3)	23.2 (12)	23.5 (7)	24.2 (8)
Na ₂ O	0.32 (5)	0.35 (6)	0.34 (6)	0.10 (3)	0.16 (2)	0.16 (4)	0.25 (13)	0.19 (6)	0.24 (4)
Sum ²	99.42	100.11	100.13	100.03	99.91	100.70	99.73	100.66	98.22
X _{Mg} ³	0.874	0.852	0.855	0.920	0.897	0.890	0.854	0.874	0.854
Si	1.817	1.801	1.813	1.937	1.915	1.913	1.825	1.821	1.825
Ti	0.029	0.034	0.034	0.012	0.018	0.018	0.036	0.037	0.036
Al	0.280	0.320	0.292	0.077	0.126	0.134	0.313	0.291	0.258
Cr	0.005	n.a.	n.a.	0.008	0.006	0.006	0.007	0.006	n.a.
Fe ²⁺	0.048	0.037	0.039	0.025	0.014	0.011	0.000	0.001	0.038
Fe ³⁺	0.071	0.098	0.094	0.058	0.088	0.097	0.130	0.114	0.096
Mg	0.825	0.780	0.789	0.949	0.889	0.882	0.757	0.795	0.779
Ca	0.902	0.903	0.914	0.926	0.932	0.926	0.913	0.921	0.951
Na	0.023	0.025	0.024	0.007	0.011	0.012	0.018	0.014	0.017

¹The numbers in parentheses are 2σ standard deviations, given in terms of the last unit cited.²Analyses have been recalculated to 100% anhydrous; the 'sum' row correspond to the original analytical total.³X_{Mg} calculated assuming all Fe as FeO.*n*, number of analyses; n.a., not analysed.

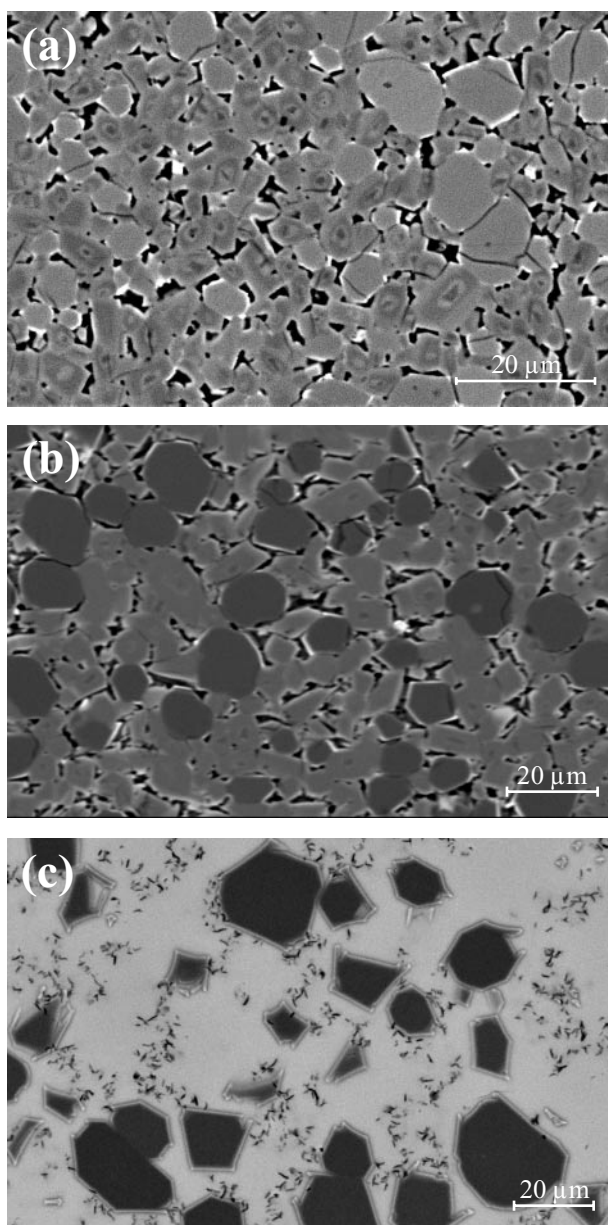


Fig. 3. Experimental textures with increasing melt fraction. Melt fractions are higher than those estimated by looking at the images, because part of the melt has been segregated into the carbon sphere layer. (a) Experiment wh15 at 0.5 GPa, 1175°C and 23% melt: one of the lowest melt fraction experiments with $<10\ \mu\text{m}$ olivine (brighter) and clinopyroxene (darker) crystals; the interstitial part corresponds to former melt and comprises quench clinopyroxene and olivine, residual glass and volatiles exsolved on quench; residual clinopyroxene cores show as small dark nuclei in some clinopyroxene crystals (see also Fig. 2b). (b) Experiment wh20 at 1 GPa, 1300°C and 56% melt: experiment showing 5–20 μm crystals of olivine (dark grey) and clinopyroxene (light grey). The interstitial part corresponds to former melt and comprises quench clinopyroxene and olivine, residual glass, and exsolved volatiles. (c) Experiment wh31 at 1 GPa, 1350°C and 77% melt: high-temperature experiment near cpx-out; 10–30 μm olivine crystals (dark grey) and rare clinopyroxene crystals (not visible on the image) in a mostly glassy experimental charge; dark dots or needles are graphite grains.

H_2 diffusion) during the experiments. Six experiments in the 12.7 mm piston cylinder assemblage, performed either with a sleeve of unfired pyrophyllite ($\sim 200\ \text{mg}$) around the platinum capsule or with short run duration, resulted in minimum water loss. For the 0.5 GPa experiments in the 19.1 mm piston cylinder assemblage (Table 3), pyrophyllite sleeves were not as efficient, probably because the latter assemblage also employs a Pyrex glass inside the graphite furnace, which acts as a sink for H_2O from dehydroxylation of pyrophyllite. The six 1.0 GPa experiments with low H_2O loss (average bulk $\text{H}_2\text{O} = 0.78$) define a good correlation between melt fraction and temperature (Fig. 5), and allow extrapolation of melt fractions to other temperatures. The other 1.0 GPa experiments plot below this correlation, and for a given temperature (e.g. at 1300°C), the experiment with the most significant water loss has the lowest melt fraction.

Nevertheless, when plotted against melt fraction, all oxides (including CaO and Al_2O_3) show very regular trends (Figs 4 and 6), suggesting that bulk water contents strongly influence melt fractions, but do not significantly displace melt compositions. Our observation is consistent with previous results: at moderate to high melt fractions, the amount of H_2O present in a mantle source mainly controls the extent of partial melting, but has little influence on the major element compositions of the partial melts at a given melt fraction (Stolper & Newman, 1994; Ulmer, 2001; Laporte *et al.*, 2004).

Melt and mineral compositions

Melt compositions are plotted as a function of melt fraction in Fig. 6. CaO contents increase with melt fraction, up to 17.6 wt % at 1.0 GPa, and to 18.2 wt % at 0.5 GPa (Fig. 6). The trend of CaO with melt fraction reaches a maximum for the highest temperature experiments, which have low abundances of clinopyroxene ($\leq 5\ \text{wt}\%$) and are probably near the cpx-out phase boundary. In contrast, Al_2O_3 concentration decreases almost linearly with melt fraction; it shows a clear dependence on pressure, with higher concentrations at 0.5 GPa as a consequence of increasing Al_2O_3 in clinopyroxene with pressure. The $\text{CaO}/\text{Al}_2\text{O}_3$ ratio strongly increases with increasing melt fraction (Fig. 6), from 0.6 at $F = 0.18$ to 1.9 at $F = 0.78$. Ultra-calcic ($\text{CaO}/\text{Al}_2\text{O}_3 > 1$) melts are obtained for experimental melt fractions exceeding 0.32, i.e. for temperatures in excess of 1190°C (Fig. 5). All the experimental melts are strongly nepheline-normative, as they have low silica and high alkali contents; normative nepheline decreases with increasing melt fraction.

Except for an increase in X_{Mg} , the compositions of residual phases show only small variations with increasing temperature. CaO concentrations in olivine range from 0.57 to 0.87 wt %, with an average of 0.74 wt % (Table 5).

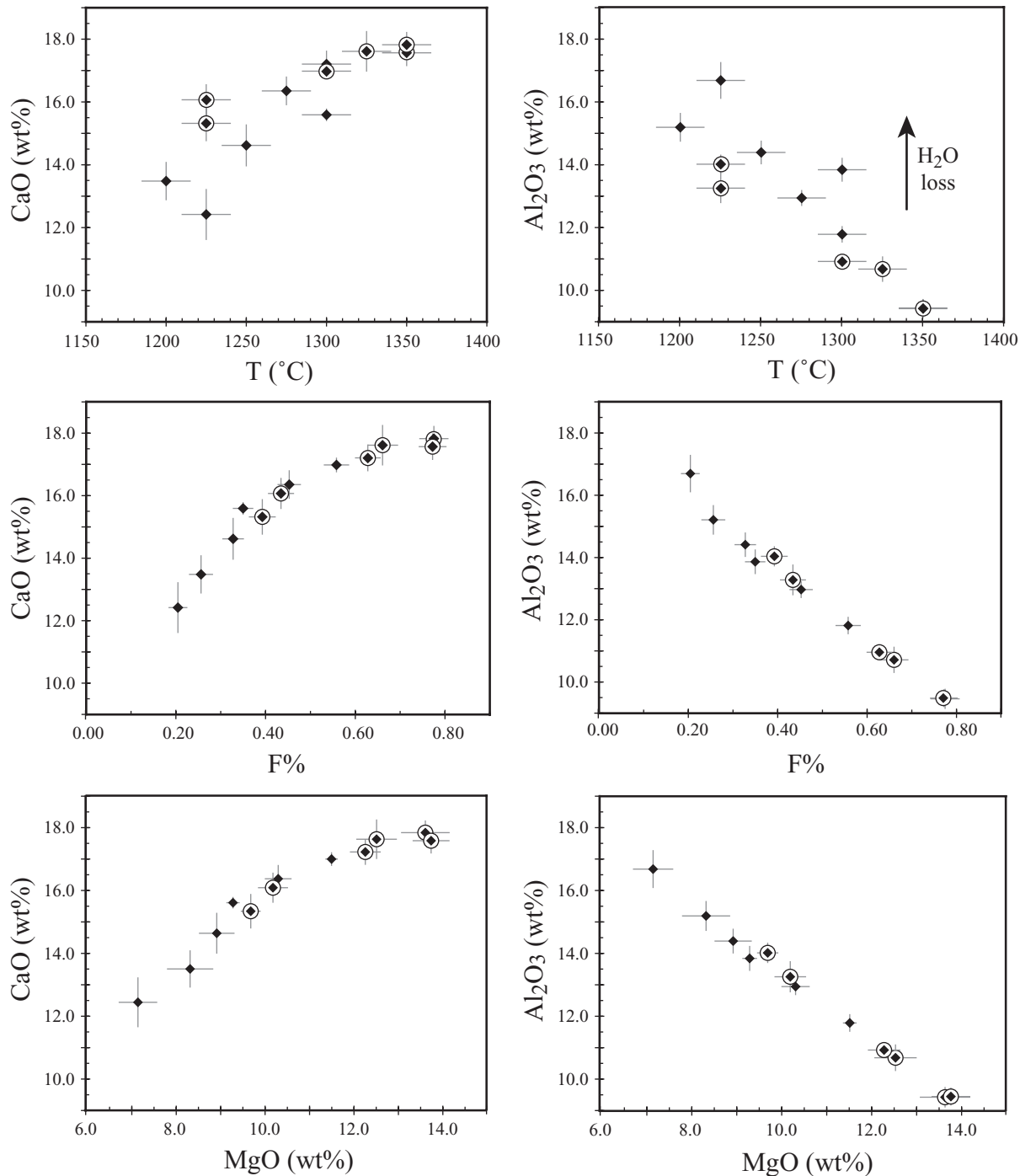


Fig. 4. Variation of CaO and Al₂O₃ concentrations (wt %) at 1 GPa as a function of temperature, melt fraction ($F\%$) and MgO content (wt %) of the partial melts. Melt fractions are calculated by mass balance, using a program developed by Albarède & Provost (1977). Error bars represent 2σ dispersion of the experimental analyses. CaO and Al₂O₃ concentrations show good correlations with MgO and F . Experiments with the lowest water losses are indicated by large circles.

Such CaO contents are slightly higher than those from other melting experiments on olivine-clinopyroxene-rich lithologies (Pickering-Witter & Johnston, 2000; Kogiso & Hirschmann, 2001; Schwab & Johnston, 2001). Higher

alkali concentrations in our partial melts compared with previous studies could explain the higher CaO contents in olivine, as Na₂O raises Ca partitioning coefficients between olivine and melt (e.g. Libourel, 1999).

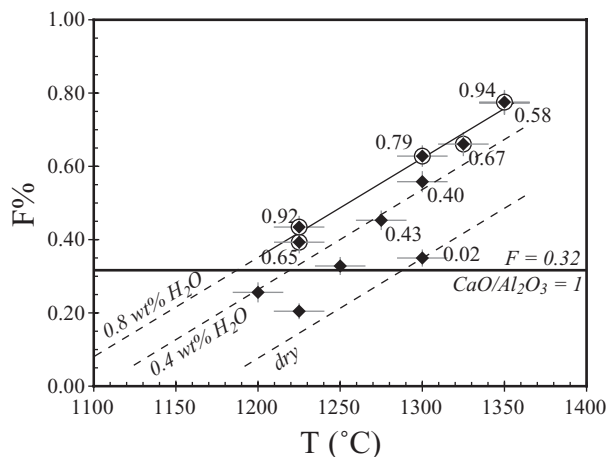


Fig. 5. Melt fraction ($F\%$) vs temperature ($^{\circ}\text{C}$) for 1.0 GPa melts. Numbers labelling the experimental points are bulk water contents, calculated from the water content of the partial melt and the melt fraction, which should be compared with the theoretical 0.8 wt % calculated from the proportion of amphibole. Melt fractions are linearly correlated with temperature at constant bulk H_2O concentration; for a given temperature, melt fraction increases continuously with bulk H_2O content. Dashed lines are estimated melt fraction vs temperature trends for three bulk H_2O contents (0.8 wt %, 0.4 wt % and dry). The three unlabelled experiments had too much quench crystallization for direct measurement of melt H_2O contents.

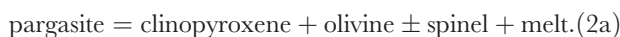
Ca concentrations in clinopyroxene remain nearly constant (Table 6, 0.88–0.95 Ca p.f.u.) and far from the two-pyroxene solvus (0.75–0.80 Ca p.f.u. at 1.0 GPa, 1200–1300 $^{\circ}\text{C}$, Brey & Huth, 1984).

Melting reactions

Proportions of glass and crystalline phases in the experiments have been determined by mass balance calculations, using an algorithm that incorporates uncertainties in bulk and phase compositions (Albarède & Provost, 1977; Table 3). Melting reactions at 0.5 and 1.0 GPa have been obtained through least-square fits of the slopes of the residual phases vs melt fraction curves (Fig. 7a) and are identical within error. At 1.0 GPa, the resulting equation for evolution along an olivine + clinopyroxene cotectic is

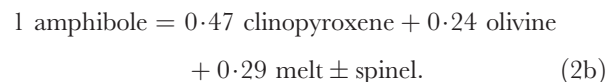
$$0.85(\pm 0.09) \text{ clinopyroxene} \\ + 0.15(\pm 0.05) \text{ olivine} = 1 \text{ melt.} \quad (1)$$

The OCA2 starting material corresponds to a mixture of olivine, clinopyroxene and amphibole, representing the subsolidus phase assemblage. When overstepping the solidus, the pargasitic amphibole melts incongruently, following the reaction (e.g. Holloway, 1972; Foden & Green, 1992; Fig. 7b)



The breakdown temperature of pargasitic amphibole has been experimentally determined in the range

1060–1110 $^{\circ}\text{C}$ (Holloway, 1972; Niida & Green, 1999). An extrapolation of our experimental temperature vs melt fraction trend (Fig. 5) down to 1100 $^{\circ}\text{C}$ leads to $\sim 10\%$ melt. The evolution of residual phase proportions with melt fraction shown in Fig. 7a suggests that 10% melt equilibrated with 28 wt % olivine and 62 wt % clinopyroxene. Such proportions can be compared with subsolidus phase proportions to give approximate coefficients for reaction (2):



We use the phase proportions in the starting material (19 wt % olivine, 45 wt % clinopyroxene and 36 wt % amphibole) as an approximation for the subsolidus phase proportions. According to the small variation of phase composition with pressure (Tables 5 and 6), the difference is assumed to be less than a few percent.

DISCUSSION

First melts from amphibole wehrlites and amphibole clinopyroxenites

Any ultramafic bulk composition constituted by melt + clinopyroxene + olivine will result in melts that evolve along a line on the clinopyroxene + olivine saturation surface. On this surface, the melting trend can be defined by two extreme compositions: (1) the composition of the lowest T melt in equilibrium with olivine and clinopyroxene only; (2) the composition of the melt when clinopyroxene (or olivine) disappears from the residue (here, close to the melt composition in experiment wh31; Table 4). It is thus important to constrain melt compositions at the starting point of the trend, i.e. exactly at the temperature where other additional minerals melt out.

Incongruent melting of amphibole

Extrapolation of melt compositions from the lowest melt fraction experiments to temperatures of amphibole breakdown ($\sim 1100^{\circ}\text{C}$) provides an estimate of melt compositions from incongruent melting of amphibole (Table 5). For this purpose we extrapolate the experimentally obtained phase proportions (1350–1200 $^{\circ}\text{C}$, Fig. 7) to 1100 $^{\circ}\text{C}$ following reaction (1), and vary olivine and clinopyroxene compositions linearly with melt fraction. FeO is poorly constrained by this model, as the FeO contents of olivine, melt and starting material are very similar, so in addition to the mass balance procedure, K_d olivine/melt is fixed at 0.30 (Roeder & Emslie, 1970) to calculate FeO concentrations in the melt. Significant uncertainties in this calculation come from possible non-linear variations of Na and Al contents in lower temperature clinopyroxenes, and mainly from the estimated

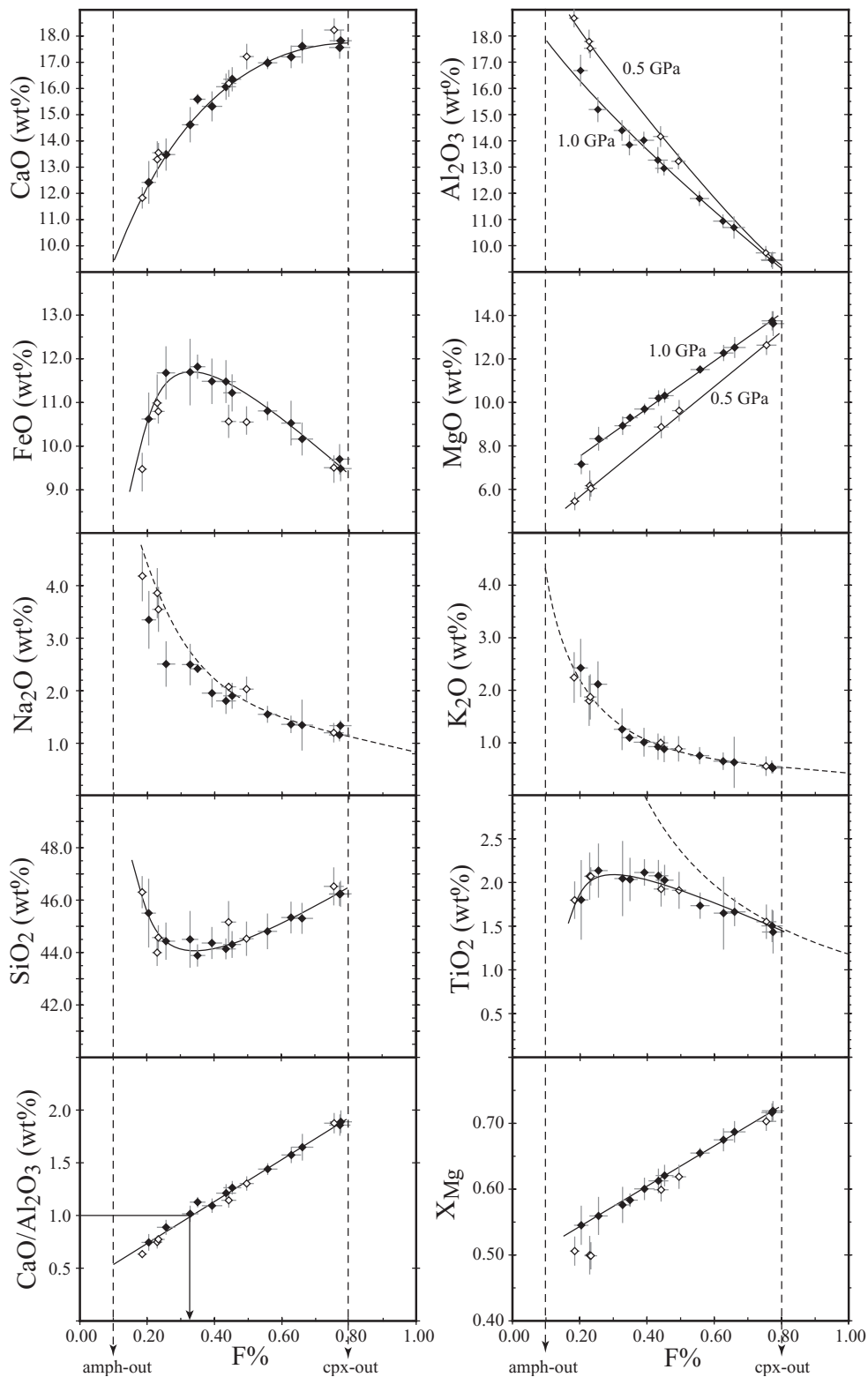


Fig. 6. Composition of glasses at 1.0 GPa (filled symbols) and 0.5 GPa (open symbols) as a function of melt fraction ($F\%$). Errors bars represent 2σ dispersion for glass compositions and 2σ dispersion propagated according to Albarède & Provost (1977) for melt fractions. Continuous curves are best fits of the data at 1.0 GPa and 0.5 GPa, whereas dashed curves are concentration vs melt fractions curves calculated assuming perfect incompatible behaviour (i.e. $D = 0$). The two vertical dashed lines indicate the approximate position of amphibole-out and clinopyroxene-out reactions.

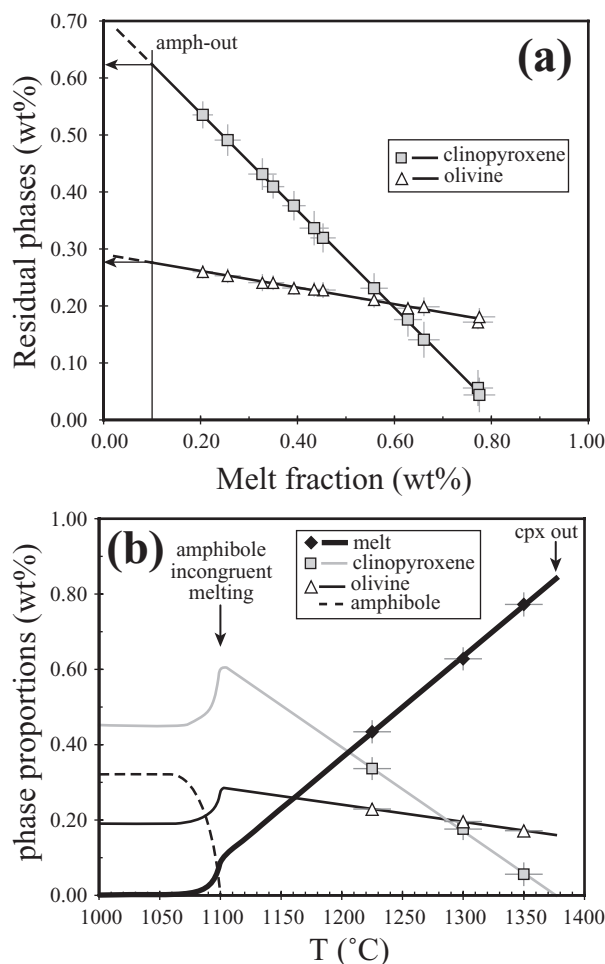


Fig. 7. (a) Change in residual phase proportions (wt %) as a function of melt fraction for the experimentally investigated composition OCA2 at 1.0 GPa. Error bars are 2σ , propagated following Albarède & Provost (1977). The continuous lines are linear least-squares fits of the phase proportions. Arrows indicate estimated phase proportions at amphibole-out. (b) Schematic melt or residual phase proportions (wt %) vs temperature diagram for amphibole wehrlite melting at 1.0 GPa. Melting is controlled by two reactions: a discontinuous reaction near 1100°C corresponding to the incongruent melting of amphibole; for temperatures $>1100^{\circ}\text{C}$, a continuous reaction following an olivine–clinopyroxene cotectic.

melt fraction at amphibole-out (see Fig. 7). The calculated melt compositions just above amphibole-out ($\sim 12\%$ melt fraction, Fig. 8, Table 7) are highly enriched in Na_2O , K_2O , and Al_2O_3 (>19.0 wt %), have SiO_2 content similar to but slightly higher than in the experimental melts from higher temperatures, and are relatively depleted in CaO (<11.0 wt %) and MgO . These compositional characteristics are in agreement with those of Holloway (1972), who argued that incongruent melting of pargasite produces melts close to the composition of a nepheline + anorthite mixture. An origin by incongruent amphibole melting has been proposed for some silicate

glasses found in lherzolite mantle xenoliths (e.g. Francis, 1976; Yaxley *et al.*, 1991; Chazot *et al.*, 1996; Ban *et al.*, 2005); these glasses are very similar to our calculated melts, except for the higher silica content of the natural glasses (47–59 wt %), which can readily be explained by interaction with orthopyroxene (Ban *et al.*, 2005).

A tentative location of cotectics for amphibole-bearing ultramafic rocks at crustal to upper mantle pressures has been drawn in Fig. 8. These are based on the well-defined cotectic for cpx + opx + ol with 3.3–6.3 wt % H_2O (Gaetani & Grove, 1998), the H_2O -saturated peritectic of amph + opx + ol on the tie-line neph–opx (Kushiro, 1974), and on the above natural melt compositions attributed to amphibole breakdown (Francis, 1976; Yaxley *et al.*, 1991; Chazot *et al.*, 1996; Ban *et al.*, 2005). Our melt composition at amphibole-out, as estimated from the experiments, roughly coincides with the amphibole + clinopyroxene + olivine peritectic based on the natural melts and marks the point of exhaustion of amphibole in our amphibole wehrlite. The main difference between our calculations and the natural melts is our elevated TiO_2 and K_2O contents; however, TiO_2 should recombine with FeO to give Ti-rich magnetite near the solidus (Ban *et al.*, 2005), which is not constrained in our mass balance, and K_2O concentrations in amphibole are highly variable. The exact composition of the first melt strongly depends on the amphibole composition, as the four phases (amphibole, olivine, clinopyroxene and melt) lie in a plane, or on an amphibole–cpx tie-line when projected from olivine. Nevertheless, most amphiboles from the mantle or primitive basalts define a restricted compositional array: they are alkali-rich and silica-poor pargasites (Fig. 8) and therefore their peritectic melts are strongly nepheline-normative.

Control on low-degree melt compositions from olivine–clinopyroxene dominant rocks

Melting of olivine–clinopyroxene-dominant rocks ('wehrlites') has been investigated by Pickering-Witter & Johnston (2000), Kogiso & Hirschmann (2001), and Schwab & Johnston (2001), using slightly different starting compositions (Fig. 9). These melting experiments share two characteristics: (1) the composition of low-degree melts is strongly controlled by the components present in addition to olivine and diopside; (2) when these additional components are melted out, melts evolve towards diopside + olivine and become ultra-calcic with increasing temperature (and melt fraction).

During low-pressure lherzolite melting, initial melts are in equilibrium with olivine + orthopyroxene + clinopyroxene \pm spinel, and then evolve along the ol + opx + cpx peritectic. In natural lherzolite, the effect of variable iron, titanium, and alkalis on melt composition is minor and experimental melts plot close to a single

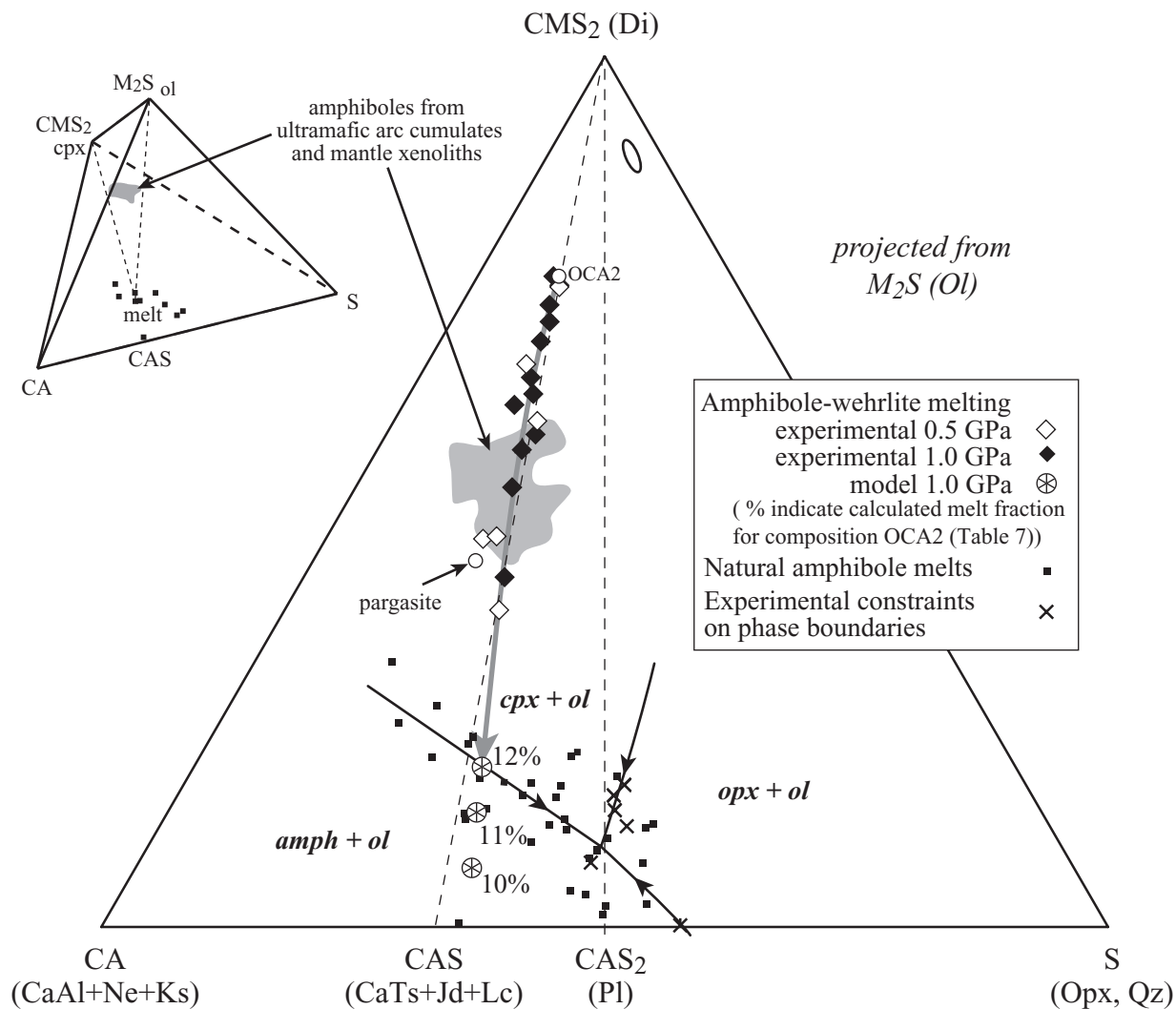


Fig. 8. Schematic CMAS phase diagram for amphibole-bearing ultramafic rocks at crustal to upper mantle pressures (0.3–1.5 GPa). The liquidus surfaces are estimated from experimental (×) and analytical (■) data: *opx*–*cpx*–*ol* under water-undersaturated conditions at 1.2 GPa from Gaetani & Grove (1998), intersection of the *opx*–*amph*–*ol* cotectic and the *Ne*–*Qz*–*Ol* plane at water-saturated conditions at 1.5 GPa after Kushiro (1974), one point on the *cpx*–*ol*–*amph* cotectic at 0.3 GPa, water-saturated conditions after Barclay & Carmichael (2004), *ol*–*cpx*–*amph* peritectic constrained by the compositions of natural glasses assumed to originate from amphibole breakdown (Francis, 1976; Yaxley *et al.*, 1991; Chazot *et al.*, 1996; Ban *et al.*, 2005). Field for pargasitic amphibole compositions in ultramafic arc cumulates and mantle xenoliths from Aoki (1971), Francis (1976), Richard (1986), Debari *et al.* (1987), Yaxley *et al.* (1991), Himmelberg & Loney (1995), Chazot *et al.* (1996), and Turner *et al.* (2003). As shown in the insert, amphibole melts incongruently to give olivine, clinopyroxene and melt; melts are thus constrained to a plane containing olivine, clinopyroxene and amphibole. In the absence of *opx*, the first melts from pargasitic amphiboles are strongly nepheline-normative. Data have been recalculated as CMAS components (O'Hara, 1968) using the following procedure: $C = (\text{CaO} - 10/3 \text{P}_2\text{O}_5 + 2 \text{Na}_2\text{O} + 2 \text{K}_2\text{O})$; $M = (\text{MgO} + \text{FeO}^* + \text{MnO})$; $A = (\text{Al}_2\text{O}_3 + \text{Na}_2\text{O} + \text{K}_2\text{O})$; $S = (\text{SiO}_2 - 2 \text{Na}_2\text{O} - 2 \text{K}_2\text{O})$; then projected from olivine (M_2S) onto the *Di*–*Ne*–*Qz* (CMS_2 –*CA*–*S*) face of the 'basalt tetrahedron'. Units used throughout the paper are molar proportions of oxides. The ellipse represents a typical analytical error.

ol + *opx* + *cpx* (three phases) control line (Fig. 9). Wehrlitic starting materials result almost immediately in melts in equilibrium with olivine + clinopyroxene (two phases only). They thus evolve from the initial melt composition towards diopside (in projection from olivine, Fig. 9) on the olivine + clinopyroxene saturation surface, which is at the *Ne* side of the *ol*–*cpx*–*opx* cotectic (Fig. 9). The initial melt composition from wehrlites, in turn, is

determined by the minor phases (amphibole, orthopyroxene, spinel), which melt out at very low melt fractions, and by minor clinopyroxene components (clinoenstatite, jadeite, *Ca*-Tschermaks), which concentrate in the melt relative to residual diopsidic clinopyroxene (diopside–*Ca*-Tschermaks: Schairer & Yoder, 1969; diopside–jadeite: Bell & Davis, 1969; diopside–enstatite: Kushiro, 1969). In particular, the above minerals or mineral components

Table 7: Composition of incongruent melts from amphiboles

	Our model (wt % melting)			Natural melts ¹
	12%	11%	10%	
SiO ₂	49.56	50.55	51.77	53.32
TiO ₂	3.36	3.50	3.66	0.61
Al ₂ O ₃	22.00	23.00	24.20	21.81
FeO*	4.21	3.10	1.76	3.51
MgO	3.08	2.28	1.30	3.11
CaO	7.73	6.52	5.03	7.97
Na ₂ O	6.10	6.69	7.41	7.05
K ₂ O	3.95	4.37	4.88	2.40

¹Representative analysis from Ban *et al.* (2005).

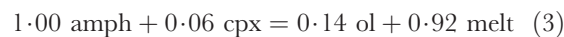
control the nepheline- or hypersthene-normative character of the initial melts. In the experiments of Schwab & Johnston (2001), the hypersthene-normative character of the initial melt (Fig. 9, INTB) reflects the presence of 7 wt % orthopyroxene in the starting material. Kogiso & Hirschmann (2001) obtained slightly nepheline-normative melts (Fig. 9, OICPx1) from a slightly nepheline-normative starting assemblage comprising Jadeite + Ca-Tschermaks enriched clinopyroxene (0.84 wt % Na₂O and 5.58 wt % Al₂O₃). In our study, the presence of pargasite, with its characteristically low SiO₂ content, imprints a strong nepheline-normative signature to the partial melts at amphibole-out (in the absence of orthopyroxene). Depending on the few percent of components extra to olivine + diopside in the 'wehrlitic' starting material, it is thus possible to obtain a large variety of melts on the olivine + clinopyroxene saturation surface, the initial hypersthene- or nepheline-normative character being retained throughout the whole melting range. By contrast, melts from lherzolites are in equilibrium with one more phase (olivine + opx + cpx), thus their composition is more constrained (one less degree of freedom).

Generation of ultra-calcic melts from amphibole-wehrlites

In previous studies, ultra-calcic melts have been obtained only at rather high degrees of melting, i.e. at >20 wt % (Pickering-Witter & Johnston, 2000; Kogiso & Hirschmann, 2001), >8 wt % (Schwab & Johnston, 2001), and temperatures exceeding 1325°C. In our experiments, the presence of amphibole in the source adds water and alkalis to the initial melts, thus greatly reducing melting temperatures: an ultra-calcic character is obtained for $F \geq 0.32$ (Fig. 5), and temperatures of

$\geq 1190^\circ\text{C}$ at 1.0 GPa (Fig. 4). The phase proportions in our starting material were chosen to obtain experimentally analysable melt proportions; however, the resulting melt compositions should not be influenced by this choice. Because of the rather small compositional variability of clinopyroxene (and olivine) during melting (Tables 5 and 6), and the small variability of mineral compositions in ultramafic arc cumulates (Table 1), phase proportions in the source can be widely varied without significantly modifying the partial melts. Thus, ultra-calcic nepheline-normative melts will be obtained for any pargasite + clinopyroxene + olivine rock (Fig. 10). Furthermore, because of the peritectic melting of pargasite [reaction (2)], melts from olivine-free amphibole-clinopyroxene cumulates will also saturate in olivine + clinopyroxene, and thus evolve along the same diopside + olivine cotectic as melts of olivine-clinopyroxene-amphibole rocks.

In the following, we use experimentally determined melting reactions to link the minimum melt fraction required to obtain ultra-calcic melts to the amphibole proportion in the source rock. For amphibole-rich (36% amphibole) assemblages, ultra-calcic melts ($\text{CaO}/\text{Al}_2\text{O}_3 \geq 1.0$) are obtained for $F \geq 32\%$. The integrated melting equation [a combination of reactions (1) and (2)] yielding melts with $\text{CaO}/\text{Al}_2\text{O}_3 = 1.0$ is



and occurs at about 1190°C (temperature estimated from a combination of the results plotted in Figs 5 and 6; see also Fig. 9). The (ultra-calcic melt)/(initial amphibole) ratio in this equation is 0.92, indicating that melts evolve to $\text{CaO}/\text{Al}_2\text{O}_3 \geq 1.0$ at melt fractions slightly less (0.92 times) than the initial amphibole proportion. The bulk melt fraction required to obtain a given $\text{CaO}/\text{Al}_2\text{O}_3$ ratio is mainly controlled by the amphibole proportion in the source. For an amphibole-poor olivine clinopyroxenite (e.g. 80BI14 in Table 1, 11 wt % amphibole), melt fractions will be proportionally lower (~10 wt % for 80BI14). In the extreme, melting of an olivine-clinopyroxene rock with minor interstitial amphibole is expected to produce ultra-calcic liquids at melt fractions below a few percent.

$\text{CaO}/\text{Al}_2\text{O}_3$ ratios in natural nepheline-normative ultra-calcic melts rarely exceed 1.25. A similar calculation shows that melt fractions ~1.3 times the initial amphibole content are necessary to reach this upper end of the compositional array of ultra-calcic nepheline-normative melts.

X_{Mg} in the melt vs X_{Mg} in the source

In this part, we show that it is possible to obtain ultra-calcic melts with an extremely wide range of X_{Mg} , similar to the natural range. Three parameters can influence the

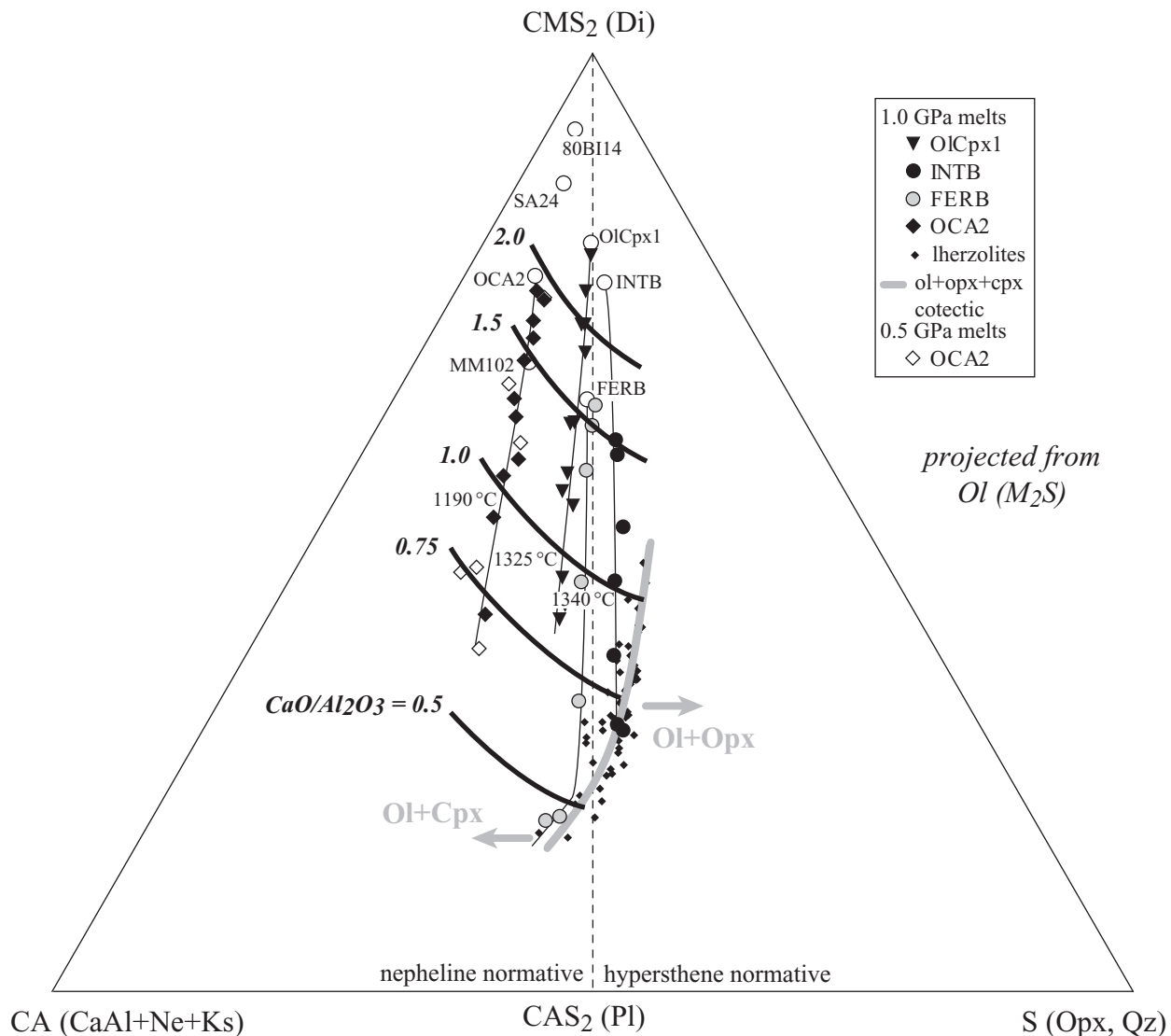


Fig. 9. Melting trends for olivine–clinopyroxene dominant rocks showing that source composition strongly controls the hypersthene- or nepheline-normative character of the partial melts. Data have been recalculated to equivalent CMAS components (O'Hara, 1968; Fig. 8) and then projected from olivine (M_2S) onto the Di–Qz–Ne (CMS_2 –S–CA) face of the 'basalt tetrahedron'. Experimental melting trends of olivine + clinopyroxene-dominant rocks at 1.0 GPa are from Pickering-Witter & Johnston (2000, FERB), Kogiso & Hirschmann (2001, OICpx1) and Schwab & Johnston (2001, INTB). Partial melts of lherzolites at 1.0 GPa from Falloon & Green (1987), Hirose & Kushiro (1993), Baker & Stolper (1994), Hirschmann *et al.* (1998), Falloon *et al.* (2001), Schwab & Johnston (2001), Wasylenki *et al.* (2003) and Laporte *et al.* (2004). The grey line represents the ol–cpx–opx cotectic defined from these experiments. FERB melting trend has been drawn to follow the olivine–clinopyroxene–orthopyroxene cotectic at the lowest temperatures, with orthopyroxene present in the experiments. ○, starting materials and natural rock compositions from Table 9. Bold black lines are curves of constant CaO/Al_2O_3 in the melt; temperatures are those required to obtain $CaO/Al_2O_3 = 1$. The low melting temperature (1190°C) for OCA2 has been estimated from combining results in Fig. 6 (32% melting to obtain $CaO/Al_2O_3 = 1$) and Fig. 5 (32% melting obtained at 1190°C with 0.8% water). The corresponding anhydrous melting temperature should be near 1290°C (Fig. 5).

X_{Mg} of the melts: (1) the oxygen fugacity (fO_2); (2) the X_{Mg} of the starting material; (3) less importantly, the olivine proportion in the source.

Our experiments have been performed at rather low fO_2 (about QFM – 2). Higher fO_2 would result in the stabilization of iron-rich spinel (magnetite), which is a common mineral in arc cumulates; this will decrease the iron content of the melt (e.g. Schmidt *et al.*, 2004) and

thus increase the X_{Mg} . Melting or crystallization of even small amounts of magnetite may have a tremendous effect on melt X_{Mg} (Fig. 11).

The X_{Mg} of our starting composition is at the lower end of the compositional array of ultramafic arc cumulates (Tables 1 and 2). In the following, we assess the influence of source X_{Mg} on melt composition using a simple model based on partition coefficients (D). The MgO

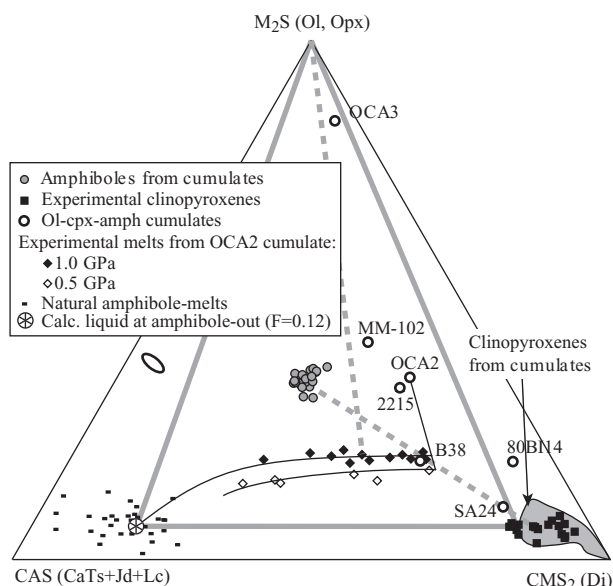


Fig. 10. Phase relations for partial melting of olivine-clinopyroxene-amphibole rocks shown in the Di-Ol-CaTs (CMS₂-M₂S-CAS) plane of the basalt tetrahedron. As clinopyroxene compositions do not vary significantly during melting, partial melts are constrained to the olivine-clinopyroxene-amphibole plane that behaves as a pseudoternary. For pargasitic amphiboles, this plane almost coincides with the Di-Ol-CaTs plane (see Fig. 9). The first melt results from incongruent amphibole melting (coexisting phases at amphibole-out indicated by wide grey lines), then the melt evolves along the olivine-clinopyroxene cotectic toward diopside-enriched (ultra-calcic) melts. Coexisting phases for CaO/Al₂O₃ = 1 [reaction (3)] are indicated by dotted grey lines. We assume a curved shape of the melting trends at low temperature, based on our modelling and the composition of natural melts from amphibole breakdown. Melt compositions obtained when linearly extrapolating the melting curves have unrealistic compositions, which are impossible to mass-balance against the starting material composition. The difference between the 0.5 and 1.0 GPa melting trends can be explained by increasing olivine solubility in the partial melts with pressure (e.g. Presnall *et al.*, 1978). Data were recalculated to equivalent CMAS (O'Hara, 1968) and then visualized from the S apex onto the CaTs-Ol-Di (CAS-M₂S-CMS₂) plane of the 'basalt tetrahedron'. Bulk and mineral compositions of arc cumulates are from Aoki (1971), Debari *et al.* (1987), Himmelberg & Loney (1995), Richard (1986), and Turner *et al.* (2003) (see Table 1). The ellipse represents the typical analytical error.

content of a partial melt is related to the MgO content of the source by

$$MgO_{source} = MgO_{melt} \cdot X_{melt} + MgO_{cpx} \cdot X_{cpx} + MgO_{ol} \cdot X_{ol} \quad (4)$$

or

$$MgO_{source} = MgO_{melt} \cdot (X_{melt} + {}^{cpx,melt}D_{MgO} \cdot X_{cpx} + {}^{ol,melt}D_{MgO} \cdot X_{ol}) \quad (5)$$

where ${}^{cpx,melt}D_{MgO} \cdot X_{cpx} = MgO_{cpx}/MgO_{melt}$. For a given source, phase proportions (X_{melt} , X_{cpx} , X_{ol}) were calculated based on a bulk melting reaction similar to (3)

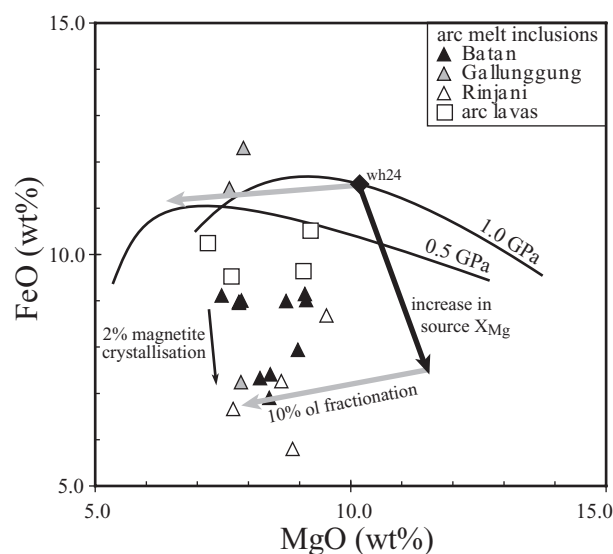


Fig. 11. Variation of FeO vs MgO (wt %) for ultra-calcic nepheline-normative melt inclusions and whole rocks compared with partial melts of OCA2 olivine-clinopyroxene-amphibole cumulate at 0.5 and 1.0 GPa (continuous curves). Most melt inclusions and whole rocks have lower FeO contents than OCA2 partial melts. However, an increase in X_{Mg} of the source results in a decrease in the FeO content of the partial melts, at almost constant MgO. Partial melts from the most magnesian cumulates have FeO contents at the lower end of the ultra-calcic melt inclusions range. Natural nepheline-normative arc ultra-calcic melts can be obtained by varying X_{Mg} in the source and by subsequent olivine fractionation.

leading to a melt with CaO/Al₂O₃ = 1.2 (wh24, average value of typical ultra-calcic melt inclusions). Using this model, melts from wehrlite MM-102 (Conrad & Kay, 1984), which represents the high- X_{Mg} end of ultramafic arc cumulates (Table 8, Fig. 11), would have $X_{Mg} = 0.742$ instead of 0.613 (OCA2). It should be noted that the X_{Mg} difference between the melts (0.742 - 0.613 = 0.129) is twice the X_{Mg} difference between the bulk compositions (0.847 - 0.782 = 0.065). With increasing X_{Mg} of the source, most of the corresponding X_{Mg} variation in the melt is accommodated by a large decrease in the FeO content of the melt, together with a lesser increase of MgO (see also Hirose & Kushiro, 1993; Kogiso & Hirschmann, 2001). This slightly raises the liquidus temperature of the ultra-calcic melt, however, by <40°C for source MM-102 relative to OCA2 (Ford *et al.*, 1983).

The same model can be employed to investigate the influence of initial phase proportions on melt X_{Mg} . For an olivine-rich composition, the X_{Mg} of the melt evolves within a small band (e.g. Baker & Stolper, 1994; Kushiro, 1996) and melts are almost in equilibrium with the initial source olivine, a buffering effect that has been widely described in lherzolite melting. For an olivine-poor composition, variation of the melt X_{Mg} is larger. This effect can be illustrated with an olivine-enriched

Table 8: Calculation of X_{Mg} of melts for varying sources

	OCA2 ¹	MM-102	OCA3
<i>Starting composition</i>			
olivine	0.19	0.20	0.80
clinopyroxene	0.45	0.28	0.10
amphibole	0.36	0.52	0.10
bulk X_{Mg}	0.789	0.847	0.803
At 1.0 GPa and 1225°C			
<i>Phase proportions (wh24)</i>			
olivine	0.229	0.257	0.811
clinopyroxene	0.337	0.109	0.067
melt	0.434	0.634	0.122
X_{Mg}			
olivine	0.846	0.909	0.814
clinopyroxene	0.874	0.926	0.847
melt	0.613	0.742	0.558
melt	MgO (wt %)	11.19	11.71
	FeO (wt %)	7.27	13.75

¹Experimental data—experiment wh24.

composition (OCA3, 80 wt % olivine), with the same phase compositions as OCA2 (Table 1). The bulk X_{Mg} of this composition is 0.017 higher than for OCA2 (0.806 vs 0.789). X_{Mg} of the initial melts are almost identical, and X_{Mg}^{melt} increases with temperature, although by much less in OCA3 (e.g. 0.558 at 1225°C) than for OCA2 with 19 wt % initial olivine (0.613 at 1225°C). The lower X_{Mg} is caused by the increased buffering capacity of olivine: X_{Mg} of olivine in OCA3 increases only from the initial 0.807 to 0.814 (at 1225°C), whereas the experiments on OCA2 yielded an increase in $X_{Mg}^{olivine}$ from 0.807 to 0.846.

Nepheline-normative ultra-calcic melts in arc settings

Comparison with the experimental melts from amphibole wehrlites

Our experiments produced nepheline-normative ultra-calcic melts at comparatively low temperatures ($\geq 1190^\circ\text{C}$). Homogenization temperatures for most nepheline-normative ultra-calcic melt inclusions preserved in olivine phenocrysts in arc basalts are in the range $1220 \pm 20^\circ\text{C}$ (Schiano *et al.*, 2000). Equilibration conditions for such melts with olivine + clinopyroxene have been determined at 1220–1320°C at 0.25–1.00 GPa under anhydrous conditions (Médard *et al.*, 2004); addition of 2.5 wt % H_2O lowers these temperatures by 50°C (Médard, 2004). The natural ultra-calcic

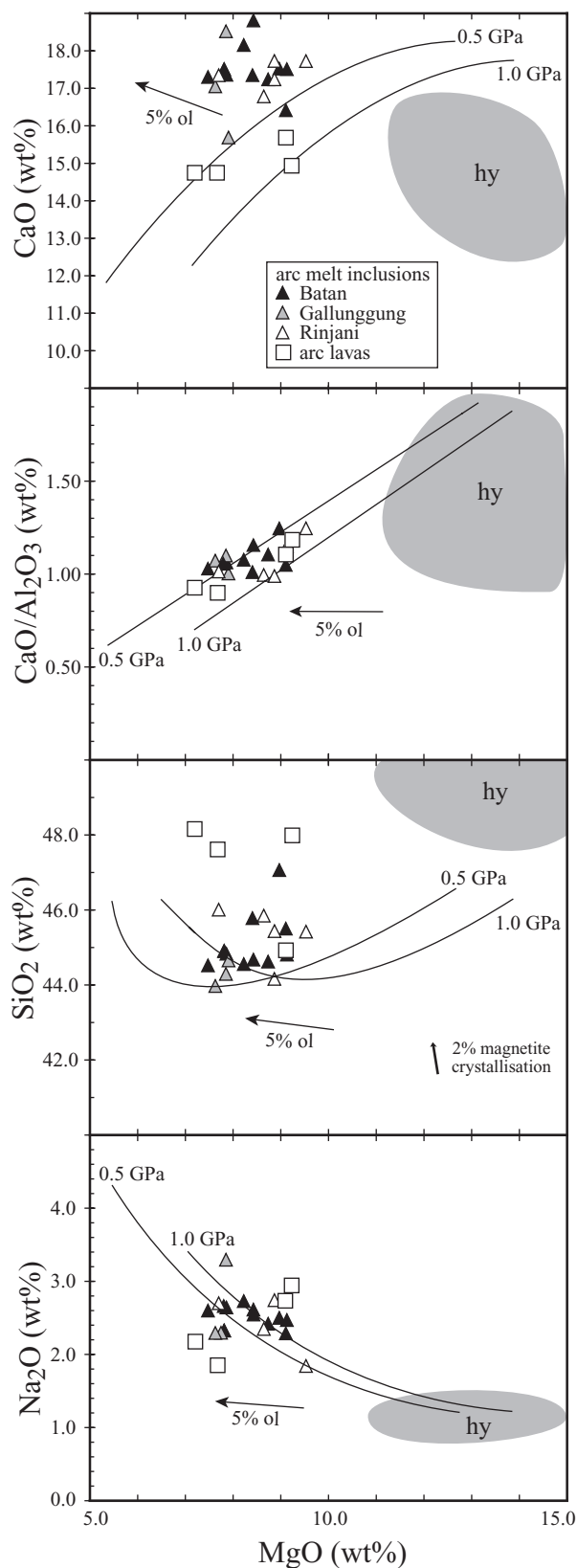
Table 9: Representative compositions of ultra-calcic nepheline-normative melt inclusions and whole rocks from arc settings

	Melt inclusions		Whole rocks	
	B7-1	48001i	L3	CR-T
SiO_2	44.02	45.49	47.35	43.74
TiO_2	0.70	0.93	0.76	1.75
Al_2O_3	16.01	14.23	12.46	13.81
FeO^*	7.31	8.57	10.36	9.39
MnO	0.12	0.14	0.21	0.15
MgO	8.30	9.54	9.12	8.87
CaO	18.54	17.76	14.73	15.26
Na_2O	2.58	1.85	2.90	2.66
K_2O	0.93	1.33	0.44	1.03
P_2O_5	n.a.	0.16	0.36	0.90
Sum	98.57	100.13	98.85	97.70

B7-1, olivine-hosted melt inclusion in basaltic lava, Batan Island, Philippines (Schiano *et al.*, 2000); 48001i, olivine-hosted melt inclusion in 'ankaramite' from Rinjani, Indonesia (Della Pasqua & Varne, 1997); L3, Ca-rich lava from Lihir, Papua New Guinea (Kennedy *et al.*, 1990); CR-T, Ca-rich lava from Nicaragua (Carr & Rose, 1984).

nepheline-normative melt inclusions and whole rocks (high-Ca basalts or 'ankaramites'; see Schiano *et al.*, 2000; Table 9) are similar to our experimental melts (Figs 12 and 13). The range of CaO (14.5–18.6 wt %) and Na_2O contents (1.8–3.3 wt %) as well as $\text{CaO}/\text{Al}_2\text{O}_3$ ratios (0.90–1.25) corresponds to the experimental melts at temperatures from 1190 to 1280°C. Differences in CaO vs MgO could be explained by ≤ 5 wt % olivine fractionation from the parental melt. The SiO_2 contents of the experimental melts (44.0–47.0 wt %) are consistent with the ultra-calcic melt inclusions and lavas (44.0–48.0 wt %). These observations suggest an origin for nepheline-normative ultra-calcic melts by partial melting of amphibole–olivine–clinopyroxene rocks in or at the base of the arc crust. As amphibole melts incongruently, producing residual clinopyroxene (i.e. a phase with high $\text{CaO}/\text{Al}_2\text{O}_3$, Holloway, 1972; Foden & Green, 1992), partial melts from amphibole will only have $\text{CaO}/\text{Al}_2\text{O}_3 < 1$; thus, the association amphibole + clinopyroxene is a prerequisite for the generation of nepheline-normative ultra-calcic melts.

The most significant discrepancy between the natural melts and our experimental melts lies in the FeO content (or X_{Mg}). Ultra-calcic nepheline-normative melt inclusions have less FeO than the experimental melts and their X_{Mg} values are up to 0.1 higher. However, we have chosen one particular starting material within a vast



range of ultramafic arc cumulates differing in X_{Mg} and by the presence of minor phases (magnetite, spinel, phlogopite). The above model (see also Fig. 11) demonstrates that variation in X_{Mg} , olivine abundance in the source, and also magnetite crystallization or melting, could explain the observed Fe/Mg range of natural nepheline-normative ultra-calcic melts. Whereas most natural nepheline-normative ultra-calcic melts have normative olivine contents similar to partial melts of amphibole wehrlites near 1.0 GPa, some of the natural melts are poorer in normative olivine than the experimental melts. As the amount of olivine in equation (3) should strongly depend on pressure (Fig. 10), analogous to lherzolite melting (Presnall *et al.*, 1978; Falloon & Green, 1988), this suggests that the natural melts are either generated at very low pressure or have fractionated some olivine before entrapment.

Finally, it is important to emphasize that the presence of H_2O in amphibole is necessary, but not sufficient to produce ultra-calcic melts at relatively low temperatures. In this study, a CaO/Al_2O_3 of 1.21 is reached at 1225°C (1.0 GPa) at 2.1 wt % H_2O in the melt (experiment wh24, Table 4). Schmidt *et al.* (2004), investigating alkali-poor hypersthene-normative ultra-calcic melts, however, obtained the same CaO/Al_2O_3 ratio only at 1300°C (1.5 GPa) with 4.1 wt % H_2O in the melt. It is thus the combined effect of H_2O and increased alkalis that reduces melting temperatures of nepheline-normative ultra-calcic melts to values that can be reached in arc settings (1180–1330°C for primary arc basalts, e.g. Tatsumi, 1982; Pichavant *et al.*, 2002).

Magma–crust interactions in subduction zones

The breakdown temperature of amphibole (1050–1100°C at 1.0 GPa; Holloway, 1972) is markedly lower than magmatic temperatures for high-Mg island arc basalts (1180–1330°C, e.g. Tatsumi, 1982; Pichavant *et al.*, 2002). Amphibole + clinopyroxene ± olivine cumulates may thus melt during intrusion of high-Mg basalts in the arc crust, and generate nepheline-normative ultra-calcic liquids at $T \geq 1190^\circ C$. As thermal diffusion is

Fig. 12. Variation diagrams comparing the composition of nepheline-normative ultra-calcic melt inclusions and whole rocks with melting trends for the olivine–clinopyroxene–amphibole composition OCA2 at 0.5 and 1.0 GPa (black lines; the length of the lines is equivalent to the experimental range). Some olivine fractionation is required to obtain the highest CaO contents of the melt inclusions, whereas the ultra-calcic arc lavas are very similar to the experimental melts. Ultra-calcic compositions are taken from Carr & Rose (1984), Thirlwall & Graham (1984), Kennedy *et al.* (1990), Della-Pasqua & Varne (1997), Métrich *et al.* (1999), Schiano *et al.* (2000) and de Hoog *et al.* (2001); these have >13.5 wt % CaO and $CaO/Al_2O_3 > 1.0$. The field of hypersthene-normative ultra-calcic melt inclusions and lavas (hy) is also plotted for comparison (see Kogiso & Hirschmann, 2001, and references therein).

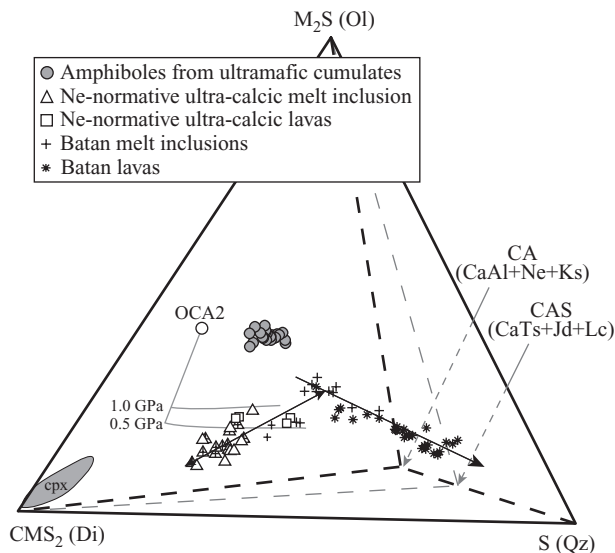


Fig. 13. 3D-molecular plot into the ‘basalt tetrahedron’ comparing nepheline-normative ultra-calcic melts from arc settings, partial melts of amphibole wehrlites and minerals from ultramafic arc cumulates. Mineral composition of arc cumulates are from Aoki (1971), Richard (1986), Debari *et al.* (1987), Himmelberg & Loney (1995) and Turner *et al.* (2003). Ultra-calcic nepheline-normative melt inclusions and whole rocks are from Carr & Rose (1984), Thirlwall & Graham (1984), Kennedy *et al.* (1990), Della-Pasqua & Varne (1997), Métrich *et al.* (1999), Schiano *et al.* (2000) and de Hoog *et al.* (2001). Nepheline-normative melts can be produced from a melting reaction in the amphibole cumulate of the type $\text{amph} + \text{cpx} = \text{ol} + \text{melt}$ (Fig. 10). Melt inclusion and whole-rock compositions from Batan Island lavas (Richard, 1986; Métrich *et al.*, 1999; Schiano *et al.*, 2000) are also plotted for comparison. The two arrows indicate the lava differentiation trend and the mixing trend between ultra-calcic melts and basaltic melts.

orders of magnitude faster than chemical diffusion (e.g. Kirkpatrick, 1981), the wall-rocks may melt as a closed system before any chemical interaction with the incoming magma occurs (e.g. Grove *et al.*, 1988). Subsequent mixing of the nepheline-normative ultra-calcic melts with the basaltic magma occurs in a zone where the magma cools and crystallizes olivine, thus producing favourable conditions for melt inclusion entrapment (e.g. Schiano, 2003). Melt inclusions in a basalt sample from Batan Island (Philippines, Schiano *et al.*, 2000; Fig. 13) record a mixing line between extreme ultra-calcic melts and a basaltic melt, which is also parental to the Batan magmatic series. Ultracalcic melt inclusions, together with other ‘anomalous’ melt inclusions (e.g. Della-Pasqua *et al.*, 1995) could thus trace melting within the cumulate pile in arcs, and in particular the role of amphibole, which lowers melting temperatures.

Potential role of amphibole-wehrlites in the genesis of nepheline-normative lavas

At a macro-scale, the melting + mixing processes recorded by melt inclusions correspond to an assimilative

process. Assimilative recycling, i.e. assimilation of previous cumulates from the same volcanic edifice, has been recorded by petrological and mineralogical investigations (e.g. Dungan & Davidson, 2004), although this process is rarely identified in whole-rock studies, as it does not modify isotopic characteristics, and may have little influence on trace and major elements as well. The presence of ultra-calcic or high-Al melt inclusions (similar to our calculated amphibole-melts) in many subduction-zone volcanoes (e.g. Della-Pasqua *et al.*, 1995; Della-Pasqua & Varne, 1997; Schiano *et al.*, 2000) indicates that assimilative recycling is widespread in arc settings. With increasing amount of secondary melts from cumulates, the nepheline-normative ultra-calcic character may affect whole-rock compositions, as in the Grenada calcium-rich lavas (Thirlwall & Graham, 1984; Figs 12 and 13, Table 9) that contain olivine–clinopyroxene–amphibole xenoliths (Arculus & Wills, 1980). It might even be possible to melt olivine–clinopyroxene–amphibole rocks in amounts sufficient for the magma to reach the surface and generate nepheline-normative ultra-calcic lavas. Lavas from Lihir Island (Papua New Guinea, Kennedy *et al.*, 1990; Figs 12 and 13, Table 9) have ultra-calcic nepheline-normative characteristics with typical subduction-zone trace element signatures, and could be an example of ultramafic cumulate melting. Indeed, amphibole-bearing olivine–clinopyroxene cumulates have been described from a nearby seamount (Franz *et al.*, 2002).

CONCLUSIONS

This study demonstrates that nepheline-normative ultra-calcic melts can be generated by melting of olivine + clinopyroxene + amphibole rocks at low temperatures ($>1190^\circ\text{C}$ at 1.0 GPa) and low melt fractions. Compared with previous studies on olivine + clinopyroxene rocks, the presence of amphibole allows production of ultra-calcic melts at temperatures that are readily achievable in the mantle or by magmatic intrusion at the base of the crust. Nepheline-normative ultra-calcic melts are clearly generated under different conditions than hypersthene-normative, depleted, ultra-calcic magmas, which require temperatures of $\geq 1350^\circ\text{C}$ to be maintained in a liquid state and originate from a refractory mantle source. Pargasitic amphibole is a key phase, as it decreases melting temperatures and imposes a nepheline-normative character to the melts.

Partial melts of our olivine–clinopyroxene–amphibole composition have strong compositional similarities to natural nepheline-normative ultra-calcic melt inclusions and whole rocks from arc settings. Phase relations suggest that nepheline-normative ultra-calcic melt inclusions in arc settings originate through the reaction $\text{amphibole} + \text{clinopyroxene} = \text{olivine} + \text{melt}$ taking place in the cumulate pile, upon intrusion of primitive basaltic magmas.

The key role of amphibole explains the occurrence of nepheline-normative ultra-calcic liquids in arcs, where H₂O-enriched magmas crystallize amphibole. These nepheline-normative ultra-calcic melts are thus tracers of magma–crust interactions, suggesting that the cumulative part of the arc crust is a common, though volumetrically minor, contaminant in island arc magma genesis.

ACKNOWLEDGEMENTS

This study has benefited from discussions with Didier Laporte, Michel Pichavant and Tim Grove. We thank Ariel Provost for his mass-balance program; Pierre Boivin for discussions on projection schemes; and Michèle Veschambre, Jean-Luc Devidal and François Faure for technical assistance with the electron probe microanalysis and SEM imaging of the experimental charges. Constructive reviews by Claude Herzberg, Tetsu Kogiso and Bruno Scaillet, as well as comments by editor Marjorie Wilson, greatly improved the manuscript. Financial support was provided by the European Community's Human Potential Programme under contract HPRN-CT-2002-00211 (Euromelt) and by INSU-CNRS (I.T. programme).

REFERENCES

- Albarède, F. & Provost, A. (1977). Petrologic and geochemical mass-balance equations: an algorithm for least-square fitting and general error analysis. *Computers and Geosciences* **3**, 309–326.
- Andrew, A. S., Hensen, B. J., Dunlop, A. C. & Agnew, P. D. (1995). Oxygen and hydrogen isotope evidence for the origin of platinum-group element mineralization in alaskan-type intrusions at Fifield, Australia. *Economic Geology* **90**, 1831–1840.
- Aoki, K. I. (1971). Petrology of mafic inclusions from Itinome-Gata, Japan. *Contributions to Mineralogy and Petrology* **30**, 314–331.
- Arculus, R. J. (1978). Mineralogy and petrology of Grenada, Lesser Antilles island arc. *Contributions to Mineralogy and Petrology* **65**, 413–424.
- Arculus, R. J. & Wills, K. J. A. (1980). The petrology of plutonic blocks and inclusions from the Lesser Antilles island arc. *Journal of Petrology* **21**, 743–799.
- Baker, M. & Stolper, E. M. (1994). Determining the composition of high-pressure mantle melts using diamond aggregates. *Geochimica et Cosmochimica Acta* **58**, 2811–2827.
- Ban, M., Witt-Eickschen, G., Klein, M. & Seck, H. A. (2005). The origin of glasses in hydrous mantle xenoliths from the West Eifel, Germany: incongruent breakdown of amphibole. *Contributions to Mineralogy and Petrology* **148**, 511–523.
- Barclay, J. & Carmichael, I. S. E. (2004). A hornblende basalt from western Mexico: water-saturated phase relations constrain a pressure–temperature window of eruptibility. *Journal of Petrology* **45**, 485–506.
- Barsdell, M. & Berry, R. F. (1990). Origin and evolution of primitive island-arc ankaramites from Western Epi, Vanuatu. *Journal of Petrology* **31**, 747–777.
- Bell, P. M. & Davis, B. T. C. (1969). Melting relations in the system jadeite–diopside at 30 and 40 kilobars. *American Journal of Science* **267**, 17–32.
- Boettcher, A. L., Windom, K. E., Bohlen, S. R. & Luth, R. W. (1981). Low-friction, anhydrous, low- to high-temperature furnace sample assembly for piston-cylinder apparatus. *Review of Scientific Instruments* **52**, 1903–1904.
- Brey, G. & Huth, J. (1984). The enstatite–diopside solvus to 60 kbar. In: Kornprobst, J. (ed.) *Kimberlites II: the Mantle and Crust–Mantle Relationships*. Amsterdam: Elsevier, pp. 257–264.
- Carr, M. J. & Rose, W. I. (1984). CENTAM: a data base of Central American volcanic rocks. *Journal of Volcanology and Geothermal Research* **33**, 239–240.
- Chazot, G., Menzies, M. & Harte, B. (1996). Silicate glasses in spinel lherzolites from Yemen: origin and chemical composition. *Chemical Geology* **134**, 159–179.
- Cherniak, D. J. (2001). Pb diffusion in Cr-diopside, augite, and enstatite, and consideration of the dependence of cation diffusion in pyroxene on oxygen fugacity. *Chemical Geology* **177**, 381–397.
- Clark, T. (1980). Petrology of the Turnagain ultramafic complex, northwestern British Columbia. *Canadian Journal of Earth Sciences* **17**, 744–757.
- Conrad, W. K. & Kay, R. W. (1984). Ultramafic and mafic inclusions from Adak island: crystallization history, and implications for the nature of primary magmas and crustal evolution in the Aleutian arc. *Journal of Petrology* **25**, 88–125.
- Cross, W., Iddings, J. P., Pirsson, L. V. & Washington, H. S. (1903). *Quantitative Classification of Igneous Rocks*. Chicago, IL: University of Chicago Press.
- Debari, S., Kay, S. M. & Kay, R. W. (1987). Ultramafic xenoliths from Adagdak volcano, Adak, Aleutian Islands, Alaska: deformed igneous cumulates from the MOHO of an island arc. *Journal of Geology* **95**, 329–341.
- De Hoog, J. C. M., Mason, P. R. D. & van Bergen, M. J. (2001). Sulfur and chalcophile elements in subduction zones: constraints from a laser ablation ICP-MS study of melt inclusions from Gallunggung Volcano, Indonesia. *Geochimica et Cosmochimica Acta* **65**, 3147–3164.
- Della-Pasqua, F. N. & Varne, R. (1997). Primitive ankaramitic magmas in volcanic arcs: a melt-inclusion approach. *Canadian Mineralogist* **35**, 291–312.
- Della-Pasqua, F. N., Kamenetsky, V. S., Gasparon, M., Crawford, A. J. & Varne, R. (1995). Al-spinels in primitive arc volcanics. *Mineralogy and Petrology* **53**, 1–26.
- Devine, J. D., Gardner, J. E., Brack, H. P., Layne, G. D. & Rutherford, M. J. (1995). Comparison of microanalytical methods for estimating H₂O contents of silicic volcanic glasses. *American Mineralogist* **80**, 319–328.
- Dungan, M. A. & Davidson, J. (2004). Partial assimilative recycling of the mafic plutonic roots of arc volcanoes: an example from the Chilean Andes. *Geology* **32**, 773–776.
- Falloon, T. J. & Green, D. H. (1987). Anhydrous partial melting of MORB pyroxene and other peridotite compositions at 10 kbar and implications for the origin of primitive MORB glasses. *Mineralogy and Petrology* **37**, 181–219.
- Falloon, T. J. & Green, D. H. (1988). Anhydrous partial melting of peridotite from 8 to 35 kb and the petrogenesis of MORB. *Journal of Petrology* **29**, 379–414.
- Falloon, T. J., Danyushevsky, L. V. & Green, D. H. (2001). Peridotite melting at 1 GPa: reversal experiments on partial melt compositions produced by peridotite–basalt sandwich experiments. *Journal of Petrology* **42**, 2363–2390.
- Foden, J. D. & Green, D. H. (1992). Possible role of amphibole in the origin of andesite: some experimental and natural evidence. *Contributions to Mineralogy and Petrology* **109**, 479–493.

- Ford, C. E., Russell, D. G., Craven, J. A. & Fisk, M. R. (1983). Olivine–liquid equilibria: temperature, pressure and composition dependence of the crystal/liquid cation partition coefficients for Mg, Fe²⁺, Ca and Mn. *Journal of Petrology* **24**, 256–265.
- Francis, D. M. (1976). The origin of amphibole in lherzolite xenoliths from Nunivak Island, Alaska. *Journal of Petrology* **17**, 357–378.
- Franz, L., Becker, K.-P., Kramer, W. & Herzig, P. M. (2002). Metasomatic mantle xenoliths from the Bismarck Microplate (Papua New Guinea)—thermal evolution, geochemistry, and extent of slab-induced metasomatism. *Journal of Petrology* **43**, 315–343.
- Freda, C., Baker, D. R. & Ottolini, L. (2001). Reduction of water-loss from gold–palladium capsules during piston-cylinder experiments by use of pyrophyllite powder. *American Mineralogist* **86**, 234–237.
- Gaetani, G. A. & Grove, T. L. (1998). The influence of water on melting of mantle peridotite. *Contributions to Mineralogy and Petrology* **131**, 323–346.
- Gill, J. B. (1981). *Orogenic Andesites and Plate Tectonics*. New York: Springer.
- Green, D. H. & Ringwood, A. E. (1970). Mineralogy of peridotitic compositions under upper mantle conditions. *Physics of the Earth and Planetary Interiors* **3**, 359–371.
- Grove, T. L., Kinzler, R. J., Baker, M. B., Donnelly-Nolan, J. M. & Leshner, C. E. (1988). Assimilation of granite by basaltic magma at Burnt Lava flow, Medicine Lake volcano, northern California: decoupling of heat and mass transfer. *Contributions to Mineralogy and Petrology* **99**, 320–343.
- Helz, R. T. (1973). Phase relations of basalts in their melting ranges at $p(\text{H}_2\text{O}) = 5$ kbar as a function of oxygen fugacity. *Journal of Petrology* **14**, 249–302.
- Himmelberg, G. R. & Loney, R. A. (1995). *Characteristics and Petrogenesis of Alaskan-type Ultramafic–Mafic Intrusions, Southeastern Alaska*. US Geological Survey Professional Paper **1564**.
- Hirose, K. & Kawamoto, T. (1995). Hydrous partial melting of lherzolite at 1 GPa: the effect of H₂O on the genesis of basaltic magmas. *Earth and Planetary Science Letters* **133**, 463–473.
- Hirose, K. & Kushiro, I. (1993). Partial melting of dry peridotites at high pressures: determination of compositions of melts segregated from peridotites using aggregates of diamonds. *Earth and Planetary Science Letters* **114**, 477–489.
- Hirschmann, M. M., Baker, M. B. & Stolper, E. M. (1998). The effects of alkalis on the silica content of mantle-derived melts. *Geochimica et Cosmochimica Acta* **62**, 893–902.
- Holloway, J. R. (1972). The system pargasite–H₂O–CO₂: a model for melting of a hydrous mineral with a mixed-volatile fluid—I. Experimental results to 8 kbar. *Geochimica et Cosmochimica Acta* **37**, 351–666.
- Holloway, J. R. & Burnham, C. W. (1972). Melting relations of basalt with equilibrium water pressure less than total pressure. *Journal of Petrology* **13**, 1–29.
- Irvine, T. N. (1974). *Petrology of the Duke Island Ultramafic Complex, Southeastern Alaska*. Geological Society of America Memoir **138**.
- Jaques, A. L. & Green, D. H. (1980). Anhydrous melting of peridotite at 0–15 kb pressure and the genesis of tholeiitic basalts. *Contributions to Mineralogy and Petrology* **73**, 287–310.
- Kay, S. M. & Kay, R. W. (1985). Role of crustal cumulates and the oceanic crust in the formation of the lower crust of the Aleutian arc. *Geology* **13**, 461–464.
- Kennedy, A. K., Grove, T. L. & Johnson, R. W. (1990). Experimental and major element constraints on the evolution of lavas from Lihir Island, Papua New Guinea. *Contributions to Mineralogy and Petrology* **104**, 722–734.
- Kirkpatrick, R. J. (1981). Kinetics of crystallization of igneous rocks. In: Lasaga, A. C. & Kirkpatrick, R. J. (eds) *Kinetics of Geochemical Processes*. Washington, DC: Mineralogical Society of America, pp. 321–398.
- Kogiso, T. & Hirschmann, M. M. (2001). Experimental study of clinopyroxenite partial melting and the origin of ultra-calcic melt inclusions. *Contributions to Mineralogy and Petrology* **142**, 347–360.
- Kushiro, I. (1969). The system forsterite–diopside–silica with and without water at high pressures. *American Journal of Science* **267**, 269–294.
- Kushiro, I. (1974). Melting of hydrous upper mantle and possible generation of andesitic magma: an approach from synthetic systems. *Earth and Planetary Science Letters* **22**, 294–299.
- Kushiro, I. (1990). Partial melting of mantle wedge and evolution of island arc crust. *Journal of Geophysical Research* **95**, 15929–15939.
- Kushiro, I. (1996). Partial melting of a fertile mantle peridotite at high pressures: an experimental study using aggregates of diamond. In: Basu, A. & Hart, S. (eds) *Earth Processes: Reading the Isotopic Code*. *Geophysical Monograph, American Geophysical Union* **95**, 109–122.
- Laporte, D., Toplis, M. J., Seyler, M. & Devidal, J.-L. (2004). A new experimental technique for extracting liquids from peridotite at very low degrees of melting: application to partial melting of depleted peridotite. *Contributions to Mineralogy and Petrology* **146**, 463–484.
- Leshner, C. E. & Walker, D. (1988). Cumulate maturation and melt migration in a temperature gradient. *Journal of Geophysical Research* **93**, 10295–10311.
- Libourel, G. (1999). Systematics of calcium partitioning between olivine and silicate melt: implications for melt structure and calcium content of magmatic olivine. *Contributions to Mineralogy and Petrology* **136**, 63–80.
- Médard, E. (2004). *Genèse de magmas riches en calcium dans les zones de subduction et sous les rides médio-océaniques: approche expérimentale*. Ph.D. thesis, Université Blaise Pascal, Clermont-Ferrand, 238 pp.
- Médard, E., Schmidt, M. W. & Schiano, P. (2004). Liquidus surfaces of ultra-calcic primitive melts: formation conditions and sources. *Contributions to Mineralogy and Petrology* **148**, 201–215.
- Métrich, N., Schiano, P., Clocchiatti, R. & Maury, R. C. (1999). Transfer of sulfur in subduction settings: an example from Batan Island (Luzon volcanic arc, Philippines). *Earth and Planetary Science Letters* **167**, 1–14.
- Niida, K. & Green, D. H. (1999). Stability and chemical composition of pargasitic amphibole in MORB under upper mantle conditions. *Contributions to Mineralogy and Petrology* **135**, 18–40.
- O'Hara, M. J. (1968). The bearing of phase equilibria studies in synthetic and natural systems on the origin and evolution of basic and ultrabasic rocks. *Earth-Science Reviews* **4**, 60–133.
- O'Neill, H. S. C. (1987). Quartz–fayalite–iron and quartz–fayalite–magnetite equilibria and the free energy of formation of fayalite (Fe₂SiO₄) and magnetite (Fe₃O₄). *American Mineralogist* **72**, 67–75.
- O'Reilly, S. Y. & Griffin, W. L. (1988). Mantle metasomatism beneath western Victoria, Australia: I. Metasomatic processes in Cr-diopside lherzolites. *Geochimica et Cosmochimica Acta* **52**, 433–447.
- Ottolini, L., Bottazzi, P., Zanetti, A. & Vannucci, R. (1995). Determination of hydrogen in silicates by secondary ion mass spectrometry. *Analyst* **120**, 1309–1313.
- Ottolini, L., Camara, F., Hawthorne, F. C. & Stirling, J. (2002). SIMS matrix effects in the analysis of light elements in silicate minerals: comparison with SREF and EMPA data. *American Mineralogist* **87**, 1477–1485.
- Parkinson, I. J. & Arculus, R. J. (1999). The redox state of subduction zones: insights from arc-peridotites. *Chemical Geology* **160**, 409–423.
- Pichavant, M., Mysen, B. O. & Macdonald, R. (2002). Source and H₂O content of high-MgO magmas in island arc settings: an experimental study of a primitive calc-alkaline basalt from St. Vincent, Lesser Antilles arc. *Geochimica et Cosmochimica Acta* **66**, 2193–2209.

- Pickering-Witter, J. M. & Johnston, A. D. (2000). The effects of variable bulk composition on the melting systematics of fertile peridotitic assemblages. *Contributions to Mineralogy and Petrology* **140**, 190–211.
- Presnall, D. C., Dixon, S. A., Dixon, J. R., O'Donnell, T. H., Brenner, N. L., Schrock, R. L. & Dycus, D. W. (1978). Liquidus phase relations on the join diopside–forsterite–anorthite from 1 atm to 20 kbar: their bearing on the generation and crystallization of basaltic magma. *Contributions to Mineralogy and Petrology* **66**, 203–220.
- Richard, M. (1986) Géologie et pétrologie d'un jalon de l'arc Taïwan–Luzon: l'île de Batan (Philippines). Ph.D. thesis, Université de Bretagne Occidentale, Brest, 351 pp.
- Roeder, P. L. & Emslie, R. F. (1970). Olivine–liquid equilibrium. *Contributions to Mineralogy and Petrology* **19**, 275–289.
- Schairer, J. F. & Yoder, H. S. (1969). Critical planes and flow sheet for a portion of the system CaO–MgO–Al₂O₃–SiO₂ having petrological implications. In: *Annual Report of the Directory of the Geophysical Laboratory*. Washington, DC: Carnegie Institution, pp. 202–214.
- Schiano, P. (2003). Primitive mantle magmas recorded as silicate melt inclusions in igneous minerals. *Earth-Science Reviews* **63**, 121–144.
- Schiano, P., Eiler, J. M., Hutcheon, I. D. & Stolper, E. M. (2000). Primitive CaO-rich, silica-undersaturated melts in island arcs: evidence for the involvement of clinopyroxene-rich lithologies in the petrogenesis of arc magmas. *Geochemistry, Geophysics, Geosystems* **1**, 1999GC0000032.
- Schiano, P., Clocchiati, R., Boivin, P. & Médard, E. (2004). The nature of melt inclusions inside minerals in an ultramafic cumulate from Adak volcanic center, Aleutian arc: implications for the origin of high-Al basalts. *Chemical Geology* **203**, 169–179.
- Schmidt, M. W., Green, D. H. & Hibberson, W. O. (2004). Ultra-calcic magmas generated from Ca-depleted mantle: an experimental study on the origin of ankaramites. *Journal of Petrology* **45**, 531–554.
- Schwab, B. E. & Johnston, A. D. (2001). Melting systematics of modally variable, compositionally intermediate peridotites and the effects of mineral fertility. *Journal of Petrology* **42**, 1789–1811.
- Snoke, A. W., Quick, J. E. & Bowman, H. R. (1981). Bear Mountain igneous complex, Klamath Mountains, California: an ultrabasic to silicic calc-alkaline suite. *Journal of Petrology* **22**, 501–552.
- Sobolev, A. & Chaussidon, M. (1996). H₂O concentrations in primary melts from supra-subduction zones and mid-ocean ridges: implications for H₂O storage and recycling in the mantle. *Earth and Planetary Science Letters* **137**, 45–55.
- Stolper, E. M. & Newman, S. (1994). The role of water in the petrogenesis of Mariana trough magmas. *Earth and Planetary Science Letters* **121**, 293–325.
- Tatsumi, Y. (1982). Origin of high-magnesian andesites in the Setouchi volcanic belt, southwest Japan II. Melting phase relations at high pressures. *Earth and Planetary Science Letters* **60**, 305–317.
- Tatsumi, Y., Arai, R. & Ishizaka, K. (1999) The petrology of a melilite–olivine nephelinites from Hamada, SW Japan. *Journal of Petrology* **40**, 497–509.
- Taylor, H. P., Jr (1967) The zoned ultramafic complexes of southeastern Alaska. In: Wyllie, P. J. (ed.) *Ultramafic and Related Rocks*. New York: John Wiley, pp. 96–118.
- Thirlwall, M. F. & Graham, A. M. (1984). Evolution of high-Ca, high-Sr C-series basalts from Grenada, Lesser Antilles: the effects of intra-crustal contamination. *Journal of the Geological Society, London* **141**, 427–445.
- Turner, S., Foden, J., George, R., Evans, P., Varne, R., Elburg, M. & Jenner, G. (2003). Rates and processes of potassic magma evolution beneath Sangeang Api volcano, East Sunda arc, Indonesia. *Journal of Petrology* **44**, 491–515.
- Ulmer, P. (2001). Partial melting in the mantle wedge—the role of H₂O in the genesis of mantle-derived 'arc-related' magmas. *Physics of the Earth and Planetary Interiors* **127**, 215–232.
- Walter, M. J. (1998). Melting of garnet peridotite and the origin of komatiite and depleted lithosphere. *Journal of Petrology* **39**, 29–60.
- Wasylenki, L. E., Baker, M. B., Hirschmann, M. M. & Stolper, E. M. (1996). The effect of source depletion on equilibrium mantle melting. *EOS Transactions, American Geophysical Union* **77**, F847.
- Wasylenki, L. E., Baker, M. B., Kent, A. J. R. & Stolper, E. M. (2003). Near-solidus melting of the shallow upper mantle: partial melting experiments on depleted peridotite. *Journal of Petrology* **44**, 1163–1191.
- Wendlandt, R. F. & Mysen, B. O. (1980). Melting phase relations of natural peridotite + CO₂ as a function of degree of partial melting at 15 and 30 kbar. *American Mineralogist* **65**, 37–44.
- Yaxley, G. M., Crawford, A. J. & Green, D. H. (1991). Evidence for carbonatite metasomatism in spinel peridotite xenoliths from western Victoria, Australia. *Earth and Planetary Sciences Letters* **107**, 305–317.